# *Scale Dependence of Mean Transverse Momentum Fluctuations at Top SPS Energy measured by the CERES experiment*

*and studies of gas properties for the ALICE experiment*

---

Vom Fachbereich Physik
der Technischen Universität Darmstadt

zur Erlangung des Grades
eines Doktors der Naturwissenschaften
(Dr. rer. nat.)

genehmigte Dissertation von

**Georgios Karolos Tsiledakis**

aus Bologna

Darmstadt 2005
D17

Referent: Prof. Dr. P. Braun-Munzinger

Koreferent: Prof. Dr. Dr./h.c.(RUS) D.H.H. Hoffmann

Tag der Einreichung: 28.Nov.2005

Tag der Prüfung: 08.Feb.2006

*Boredom and impatience are the most immoral emotions there can be. For man sets time as real in them: he wants it to pass without him having to fill it, without it being mere phenomenal form of his inner liberation and extension, mere form in which he must strive to be realised, but rather independent from him, and he dependent on it. Boredom is at the same time the need to annul time from outside, and the longing for the devil's work.*

Otto Weininger (1880-1903)

# *Summary*

The principal aim of the study of ultrarelativistic nucleus-nucleus collisions is the search for evidence of a transient state of deconfined quarks and gluons in the early, dense and hot stage of the reaction. Non-statistical event-by-event fluctuations of mean transverse momentum, $p_T$, have been proposed as a possible signature for the QCD phase transition, in particular for the critical point. However, the magnitude of the measured fluctuations is not as large as anticipated. Since fluctuations were characterized so far by one single (integral) number, it was difficult to estimate the many possible contributions to them.

Taking into account the high available statistics offered by the CERES experiment combined with the full azimuthal acceptance, a differential study of mean $p_T$ fluctuations is performed, which provides the sensitivity to discriminate among various correlation sources. For the first time at SPS energy, the charge-dependent mean $p_T$ fluctuations have been analyzed as a function of the angular pair separation, $\Delta\phi$, and of the separation in pseudorapidity, $\Delta\eta$. Thus, we are able to show that the overall fluctuations are dominated by the short range correlation peak at small opening angles ('near-side'), most probably originating from Bose-Einstein and Coulomb effects between pairs of particles emitted with similar velocities. Another important contribution is a broad maximum at $\Delta\phi$=180$^o$ ('away-side') originating from back-to-back (jet-like) correlations. Since the fluctuations related to the critical point should be present for all opening angles the best strategy is to focus on the fluctuations in the region of $30^o < \Delta\phi < 60^o$, free of the influence of the two mentioned components, and where the elliptic flow cancels out. Concerning the observed away-side peak, we demonstrate that it comes from high-$p_T$ correlations that cannot be attributed to the elliptic flow.

The second part of the thesis is dedicated to studies of gas properties for the ALICE experiment at the CERN LHC. Drift velocity and gain measurements have been performed for a number of gas mixtures in order to assess the effect of nitrogen which is expected to accumulate in the gas volume over long periods of running. The ALICE Transition Radiation Detector (TRD) is designed to work with a gas of 85 % Xe and 15 % $CO_2$. Some of the nine isotopes of Xe have very

high neutron capture cross-section leading to multi-gamma deexcitation cascades which produce background for the physical signals. An exhaustive study of this issue based on Monte Carlo simulations is presented, demonstrating that the level of this background is low enough not to cause deterioration in the performance of the detector. In addition, the resulting radioactivity and dose rate of the active gas system of ALICE TRD activated by slow neutrons is investigated and appear to be low and safe.

# *Zusammenfassung*

Für stark wechselwirkende Materie wird bei hoher Temperatur und/oder Dichte die Existenz einer Phase erwartet, in welcher der Einschluss von Quarks und Gluonen in Hadronen (Confinement) aufgehoben ist. Erzeugung und Nachweis dieses Materiezustands soll durch das Studium von Kollisionen schwerer Ionen erbracht werden. Als mögliche Signatur für den Phasenübergang, insbesondere für einen möglichen kritischen Punkt, wurden nicht-statistische event-by-event Fluktuationen des mittleren Transversalimpulses $p_T$ diskutiert. Die Stärke des beobachteten Signals ist allerdings geringer als erwartet. Bisher wurden Fluktuationen nur durch gemittelte Grössen charakterisiert, so dass eine systematische Untersuchung unterschiedlicher Beiträge nur schwer durchführbar war.

In dieser Arbeit werden Fluktuationen des mittleren Transversalimpulses anhand von Daten des CERES Experiments untersucht. Die volle azimuthale Akzeptanz des Experiments sowie die hohe Anzahl an erfassten Kollisionsereignissen erlaubt es, im Rahmen einer differentiellen Analyse verschiedene Beiträge zu den gemessenen Korrelationen zu identifizieren. Wir präsentieren, zum ersten Mal für SPS Energien, eine Studie der Transversalimpulsflukutationen in Abhängigkeit vom Öffnungswinkel $\Delta\phi$, der Separation in Pseudorapidität $\Delta\eta$ und der Ladung der korrelierten Paare. Wie sich herausstellt sind die gemessenen Fluktuationen durch kurzreichweitige Korrelationen bei kleinem Öffnungswinkel dominiert, in denen sich höchstwahrscheinlich Bose-Einstein Korrelationen und Coulomb-Wechselwirkung zwischen Teilchenpaaren ähnlicher Geschwindigkeit manifestieren. Weiterhin finden wir ein breites Maximum für $\Delta\phi$=180°, deren Ursprung in 'back-to-back' (jetartigen) Korrelationen liegt. Da Fluktuationen in Zusammenhang mit dem Phasenübergang für beliebige Öffnungswinkel erwartet werden, schlagen wir als Signatur für den kritischen Punkt Transversalimpulsfluktuationen im Winkelbereich $30° < \Delta\phi < 60°$ vor, da für diese Öffnungswinkel die diskutierten Komponenten nicht beitragen, ebensowenig wie Korrelationen durch kollektive Effekte im Feuerball (elliptischer Fluss). Weiterhin wird demonstriert, dass die Korrelation für $\Delta\phi$=180° bei hohem Transversalimpuls nicht auf elliptischen Fluss zurückzuführen ist.

Der zweite Teil der vorliegenden Arbeit widmet sich der Untersuchung von Eigenschaften von Gasen, die im ALICE Detektor am CERN LHC eingesetzt werden sollen. Für eine Reihe von Gasmischungen wurden Messungen der Ladungsverstärkung und Driftgeschwindigkeiten von Elektronen durchgeführt, um den Einfluss der Anreicherung von Stickstoff über längere Strahlzeitperioden zu untersuchen.

Der ALICE Transition Radiation Detector (TRD) operiert mit einem Gasgemisch aus Xe(85 %) und $CO_2$(15 %). Einige der insgesamt neun stabilen Xenon-Isotope haben hohe Wirkungsquerschnitte für Neutroneneinfang, der zu Gamma-Kaskaden beim Übergang der angeregten Tochterkerne in den Grundzustand führt. Solche Gammastrahlung stellt störenden Untergrund für den Detektor dar. Mittels umfangreicher Monte-Carlo Simulationen können wir demonstrieren, dass der Beitrag durch solchen Untergrund gering ist und die Funktion des Detektors nicht beeinträchtigt ist. Darüberhinaus wird die Dosisrate durch langsame Neutronen innerhalb des ALICE TRD Gassystems bestimmt und gezeigt, dass diese als gering und ungefährlich einzustufen ist.

# Contents

# Chapter 1

# Preface

Quantum Chromodynamics (QCD) predicts that strongly interacting matter can exist in different phases. The expectation is that at high enough temperature and/or density hadrons dissolve into a new form of elementary particle matter, the Quark-Gluon Plasma (QGP), where quarks and gluons are deconfined. At this phase transition it is expected that chiral symmetry is restored, with significant consequences on particle properties. The goal of heavy-ion collision experiments is to shed light on the thermodynamic properties of strongly interacting matter under these conditions and to investigate the QCD phase diagram.

As fluctuations are sensitive to the dynamics of the system, the analysis of event-by-event fluctuations of the mean transverse momentum has been proposed as a tool to search for the phase transition, especially the QCD critical point via their non-monotonic variation with control parameters such as beam energy and centrality.

In fact, significant non-statistical event-by-event fluctuations and a characteristic centrality dependence have been observed over a wide range of beam energies at different experiments. However, the magnitude of the measured fluctuations is not as large as anticipated.

This work extends the previous study [45] of the CERES experiment of event-by-event transverse momentum fluctuations. The main objective is to resolve them as a function of the angular pair separation, $\Delta\phi$, and of the separation in pseudo-rapidity, $\Delta\eta$. This 'differential', scale-dependent analysis, which is presented for the first time at SPS energy, will be compared with two-particle

transverse momentum correlations in order to extract complete information that will be studied to shed light on their origin.

The thesis is structured as follows: Chapter 2 introduces the physics topics discussed in this work. In Chapter 3 the statistical tools used in this analysis are introduced and briefly discussed. The previously published results on fluctuations are presented in Chapter 4. The experimental set-up of CERES as well as the data analysis is decribed in Chapter 5. In Chapter 6 we present and discuss the results of the scale dependence of mean transverse momentum fluctuations.

The second part of the thesis is dedicated to studies of gas properties for the ALICE experiment. A short description of the ALICE experiment is given in Chapter 7. Measurements of drift velocities and gains in gas mixtures based on Ar and Xe, with $CO_2$, $CH_4$, and $N_2$ as quenchers, are presented in Chapter 8. Finally, the radiation background which will be present in the real LHC environment as well as an estimate of the activity levels of the gas system of the ALICE TRD (Transition Radiation Detector) as calculated by detailed Monte Carlo simulations are discussed in Chapter 9.

# Part I

# Chapter 2

# Introduction

Ultra-relativistic heavy ion collisions offer the unique opportunity to probe highly excited (dense) nuclear matter under controlled laboratory conditions. The compelling driving force for such studies is the expectation that at high enough temperature and/or density hadrons dissolve into a new form of elementary particle matter, the **Quark Gluon Plasma** (QGP), where quarks and gluons are deconfined. Besides this deconfinement, chiral symmetry is expected to be restored in a QGP, which means that the quark masses will approach zero. This phase transition is predicted by Quantum Chromodynamics (QCD), the theory of strong interactions. The opposite phase transition, from quarks and gluons to hadronic matter, took place about $10^{-5}$ s after the Big Bang, the primeval event which is at the origin of our Universe. The study of phase transitions is of crucial importance for our understanding of the early evolution of the Universe. The QCD phase transition can only be accessible to laboratory experiments in high energy heavy ion collisions [1].

## 2.1 Hot and Dense Nuclear Matter

We know (since at least 40 years) that hadrons, the particles participating in the strong interaction, such as protons, neutrons and pions, are not elementary, but are made of quarks. Quarks are fermions (spin $\frac{1}{2}$) and come in six varieties, or flavors; These are $u$ (up), $d$ (down), $c$ (charm), $s$ (strange), $b$ (bottom) and $t$ (top). According to QCD, quarks carry a strong interaction charge (colour) which comes

in three types (red, green and blue), while antiquarks carry anticolour. Quarks interact among themselves via the exchange of the colour field quanta (gluons). Gluons themselves carry a colour charge, unlike the photon in QED (Quantum Electrodynamics), which carries no electric charge. All known hadron states are colour singlets (white). These white objects can be constructed by either combining three different colours or a colour with its anticolour (baryons: $qqq$ states; mesons $q\overline{q}$ states). In particular, no free quark has ever been detected and quarks seem to be permanently confined within hadrons.

What if we compress/heat the system so much that the individual hadrons start to interpenetrate? **Lattice QCD**, which is used to address the non-perturbative aspects of QCD [2], predicts that if a system of hadrons is brought to sufficiently large density and/or temperature a deconfinement phase transition should occur. In the new phase, called **Quark Gluon Plasma** (QGP), quarks and gluons are not longer confined within individual hadrons, but are free to move around over a larger volume. Confined quarks acquire an additional mass ($\sim$ 350 MeV) dynamically through the confining effect of strong interactions. Deconfinement is expected to be accompanied by a restoration of the masses to the 'bare' values they have in the Langrangian.

The transition to free quarks and gluons is accompanied by the sudden increase of the energy density as a function of temperature, shown in Fig. 2.1 for two and three degenerate flavours [3, 4]. For the 2-flavor case, the transition occurs at a critical temperature $T_c \simeq$170 MeV with critical energy density $\varepsilon_c \simeq$0.7 GeV, while for the 3-flavor case $T_c$ is smaller by about 20 MeV. A result for the case of two degenerate flavors and a heavier strange quark (physical values) is also included. The values according to the law of Stefan-Boltzmann for an ideal gas of non-interacting quarks and gluons are indicated at the right edge of the figure. As strange quarks have mass $m_s < T_c$ they will not contribute to the thermodynamics close to $T_c$, but will do so at higher temperatures. Since all heavier quarks do not contribute in the temperature range accessible in present or forseable future heavy-ion experiments, the bulk thermodynamic observables of QCD with a realistic quark mass spectrum will essentially be given by massless 2-flavour QCD close to $T_c$ and will rapidly switch over to the thermodynamics of massless 3-flavour QCD in the plasma phase. This is indicated by the crosses of

Fig.2.1. The transition is second order in the chiral limit of 2-flavour QCD and first order for 3-flavour QCD and it is likely to be a rapid crossover in the case of the physically realized quark mass spectrum. The crossover, however, does take place in a narrow temperature interval, which means that the transition between the hadronic and plasma phase is still well localized. This is reflected in a rapid rise of energy density ($\varepsilon$ ) in the vicinity of the crossover temperature. This leads to large correlation lengths and a rapid rise in susceptibilities. These might be detectable experimentally through the event-by-event analysis of fluctuations in particle yields.

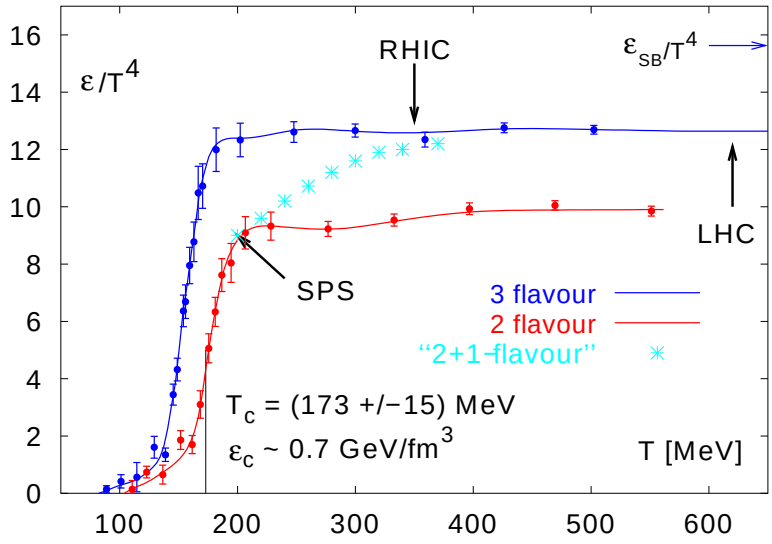


Figure 2.1: Energy density as a function of temperature calculated with lattice QCD (taken from ref.[4])

## 2.2 Experimental program and global observables

By colliding heavy ions at ultrarelativistic energies, one expects to create matter under conditions that are sufficient for deconfinement [5].

In 1985, the program has started with fixed target experiments at the CERN's Super Proton Synchrotron (SPS) which is just being concluded and at Brookhaven's

Alternating Gradient Synchrotron (AGS) which is essentially completed. The only operational heavy-ion collider is the Relativistic Heavy Ion Collider (RHIC) at Brookhaven National Laboratory (BNL) [6]. The Large Hadron Collider (LHC) will start operating at CERN in 2007 and will provide (in addition to proton beams) heavy ion beams, which will be used in the research program of the dedicated ALICE experiment.

The temporal evolution of a (central) nucleus-nucleus collision at ultrarelativistic energies is understood to proceed through the following stages: i) liberation of quarks and gluons due to the high energy deposited in the overlap region of the two nuclei; ii) equilibration of quarks and gluons; iii) crossing of the phase boundary and hadronization; iv) freeze-out.

Even if QGP is formed, as the system expands and cools down it will hadronize again, as it did at the beginning of the life of Universe: we end up with confined matter again. This is the experimental challenge: to observe in the final state the signatures of the phase transition, physical effects which are consequences of the phase transition or cannot be explained otherwise.

### 2.2.1 Collision Characteristics

In accordance with the spectator-participant model [7] of a heavy-ion collision, the participating nucleons from overlapping nuclear parts create a volume of high temperature and density, while the spectators move basically undisturbed through the collision. The impact parameter $b$ determines the centrality of the collision. The impact parameter is not directly measurable in the collisions. To determine the collision geometry, measurements of quantities which are strongly correlated to the number of participants are used, such as the transverse and forward energy and the number of produced particles. The transverse energy, $E_T$ , is defined as:

$$E_T = c^2 \sum_{i=1}^{N} (m_T)_i \tag{2.1}$$

where $i$ runs over all $N$ particles detected in an event and the transverse mass $m_T$ is given by:

$$m_T = \sqrt{m^2 + (p_T/c)^2} \tag{2.2}$$

where $p_T$ is the momentum component perpendicular to the beam direction defined as:

$$p_T = p \sin\theta \tag{2.3}$$

where $\theta$ is the polar angle of particle track. In practice, $E_T$ is measured with a segmented calorimeter and calculated as the sum of the energy $E_i$ at polar angle $\theta_i$ in each segment $(i)$:

$$E_T = \sum_{i=1}^{N} E_i \sin\theta_i \tag{2.4}$$

The rapidity $y$ is a very useful variable for description of the longitudinal motion of particles with non zero rest mass. If the particle has an energy $E$ and momentum component along the beam axis $p_z$, we can define its rapidity as:

$$y = \frac{1}{2} ln \frac{E + p_z}{E - p_z} \tag{2.5}$$

A frequently used approximation to the rapidity is the pseudorapidity $\eta$ given by:

$$\eta = -ln(\tan\frac{\theta}{2}) \tag{2.6}$$

for which it is enough to measure the polar angle $\theta$ of the particle track.

### 2.2.2 Quark-Gluon Plasma Signatures

Quarks and gluons coexisting in the short-lived QGP state cannot be measured directly and information from the early stages of the collision may get lost when the system hadronizes. Various kinds of measurements have to be combined to get reliable proof of the formation of a QGP. Specific probes of QGP (taken from ref.[3]) have been proposed [8, 9] and are currently being studied experimentally: i) direct photons [10]; ii) low-mass dileptons [11]; iii) strangeness [12, 13]; iv) charmonium suppression [14]; v) jet-quenching [15]; vi) fluctuations [16, 45]. Other global observables, like the distribution of particles over momentum space, collective flow, and the measurements of effective source sizes via particle interferometry, have also been studied in detail. A description of the ideas behind some of the most promising signatures that will be used in this work is given below.

- **Jet Quenching**

  The propagation of partons through a hot and dense medium modifies their transverse momentum due to induced radiative energy loss, a phenomenon called jet quenching [17, 18]. This can be studied by measuring the $p_T$ distribution of hadrons coming from high-$p_T$ jets. When a hard collision, producing two jets, occurs near the surface of the nuclear overlap region, jet quenching might lead to complete absorption of one of the jets, while the other escapes. This signature can be found by studying azimuthal back-to-back correlations of jets. In general, high-$p_T$ partons traveling through the dense medium is probably one of the best probes that can be used to study the medium.

- **Flow**

  As the created particles are pushed away from the hot collision region, they acquire a flow velocity pointing outwards. Their momentum increases and the transverse momentum distribution is altered. Since the flow builds up throughout the evolution of the system, it contains information on both the partonic and the hadronic stages. Anisotropic flow [19] appears in a non-central nucleus-nucleus collision. It is most conveniently quantified by the Fourier coefficients in the expansion:

  $$\frac{d^2N}{dp_T d\phi} = \frac{dN}{dp_T}(1 + 2v_1 cos(\phi) + 2v_2 cos(2\phi) + 2v_4 cos(4\phi) + ...) \qquad (2.7)$$

  displaying only the most contributing terms. Here, the $\phi$ angle is measured with respect to the reaction plane. The $v_2$ coefficient is often referred to as elliptic flow.

- **Event-by-Event Fluctuations**

  Making use of high particle multiplicities in the heavy systems at SPS and higher energies, we can extract thermodynamic properties of the system by studying several observables on an event-by-event basis. Such measurements present a clear advantage over the averaging of many events. They enable categorization of individual events into groups according to

thermodynamic properties and could potentially lead to the isolation of events with special properties associated with quark-gluon plasma formation. Phase transitions are normally associated with large fluctuations. The QGP phase transition may yield anomalous fluctuations in e.g. particle multiplicities, ratios and transverse momenta. This signature will be discussed in detail in section 2.4.

## 2.3 Searching for the QCD critical point

Thermodynamical information is often presented in the form of a **phase diagram**, in which the different manifestations or phases of a substance occupy different regions of a plot whose axes are calibrated in terms of the external conditions or control parameters [20]. The system under consideration is a region occupied by strongly interacting matter, described by QCD, in thermal and chemical equilibrium, characterized by the given values of temperature $T$ and baryo-chemical potential $\mu_b$.

Our present understanding [23] of the phases of strongly interacting matter is sketched as a $T - \mu_b$ diagram in Fig. 2.2. The exotic region of low temperatures and high densities (high $\mu_b$) is of relevance to astrophysical phenomena (neutron star physics). The region of high temperatures is the part which is being explored in ultrarelativistic nucleus-nucleus collisions. Theorists expect that this region has an interesting feature: the end point of the first order phase transition line. The critical point is marked as triangle in Fig. 2.2. The arguments leading to such picture can be summarized as follows: 1) First-principle lattice simulations indicate that no phase transition (in a strict thermodynamic sense) occurs as a function of temperature at zero baryo-chemical potential. 2) Non-lattice models indicate that transition from nuclear fluid to quark-matter (with approximate chiral symmetry restored) occurs via a strong first order transition. 3) The last step of the argument is a logical consequence of the previous two. Since the first order line originating at zero $T$ cannot end at the vertical axis $\mu_b = 0$, the line must end somewhere in the midst of the phase diagram [24].

The location of this endpoint is not yet known since the lattice predictions vary wildly. Nevertheless, the available theoretical estimates strongly indicate

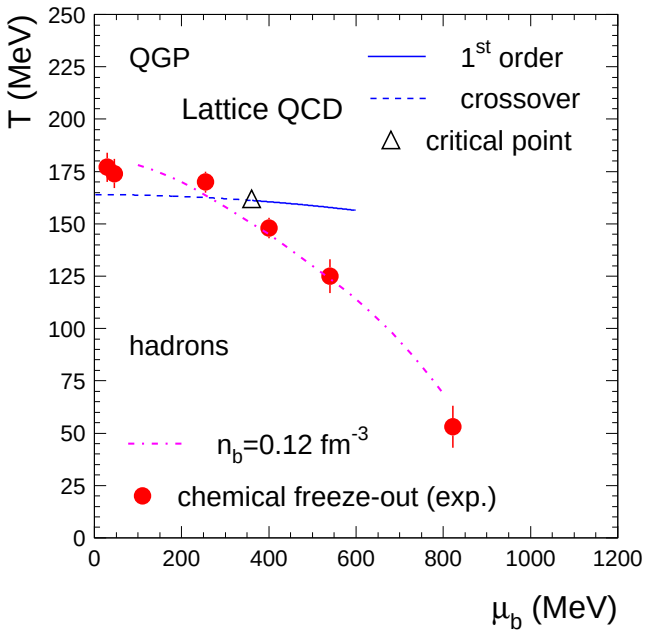


Figure 2.2: Phase diagram of nuclear matter in the temperature - baryon chemical potential plane. Experimental points for hadro-chemical freeze-out are shown together with a recent lattice QCD calculation [21] and a curve of constant total baryon density. Figure taken from ref. [22].

that the point is within the region of the phase diagram probed by the heavy-ion collision experiments. The strategy is to scan the QCD phase diagram by changing the beam energy $\sqrt{s}$. It is known empirically [22] that with increasing collision energy, $\sqrt{s}$, the resulting fireballs tend to freezeout at decreasing values of the chemical potential, since the amount of generated entropy (heat) grows with $\sqrt{s}$ while the net baryon number is limited by that number in the initial nuclei. The freeze-out points for different heavy-ion collision experiments with a recent lattice calculation superimposed can also be seen in Fig. 2.2.

## 2.4 Transverse momentum fluctuations

In general, every physical system fluctuates and in many cases these fluctuations reveal important information about the properties of the system. The magnitude of fluctuations is given by the so-called susceptibilities, which control the response of the system to the application of small external forces. Fluctuations are also closely related to phase transitions. Considering the richness of the QCD phase-diagram the study of fluctuations [25] in heavy ions physics could lead to a rich set of phenomena. The most efficient way to address fluctuations of a system created in a heavy ion collision is via the study of event-by-event (E-by-E) fluctuations, where a given observable is measured on an event-by-event basis and the fluctuations are studied over the ensemble of the events. In most cases (namely when the fluctuations are Gaussian) this analysis is equivalent to the measurement of two particle correlations over the same region of acceptance.

The passage of a system through a second order transition or close to a critical point may lead to critical phenomena, long range correlations and large fluctuations. The study of event-by-event fluctuations therefore provides a novel probe to explore the QCD phase diagram, searching for the quark-gluon plasma (QGP) and the QCD critical point. Such measurements became possible with large acceptance experiments at SPS and RHIC, where the high multiplicity of charged particles produced in collisions of lead and gold nuclei allows a precise determination of global observables on an event-by-event basis.

Transverse momentum fluctuations ($p_T$ fluctuations) should be sensitive to temperature/ energy fluctuations. These in turn provide a measure of the heat capacity of the system. Since the QCD phase transition is associated with a maximum of the specific heat, the temperature fluctuations should exhibit a minimum in the excitation function. It has also been argued that these fluctuations may provide a signal for the long range fluctuations associated with the critical point of the QCD phase diagram. In the vicinity of the critical point the transverse momentum fluctuations should increase, leading to a maximum of the fluctuations in the excitation function. It was predicted that mean $p_T$ fluctuations can be enhanced if the system passes through the QCD critical point, where long wave length fluctuations of the sigma field develop, leading to fluctuations of pions

through the strong $\sigma - \pi - \pi$ coupling [26].

In the next two Chapters 3 and 4, the proposed measures of mean $p_T$ fluctuations and the latest published results will be discussed.

# Chapter 3

# Measures of Mean $p_T$ Fluctuations

When measuring event-by-event fluctuations in heavy ion collisions, one should consider the influence of trivial sources of fluctuations. Even for tight centrality cuts there are fluctuations in the impact parameter (event-by-event fluctuations of the collision geometry) which may mask the fluctuations of interest. In the thermal language, these impact parameter fluctuations correspond to volume fluctuations. The way out is to study so called intensive variables, i.e. variables which do not scale with the volume, such as temperature, energy density etc. Another issue is the presence of statistical fluctuations due to the finite number of particles observed. These need to be subtracted in order to access the dynamical fluctuations of the system. Finally, there are fluctuations induced by the measurement/detector, which also contribute to the signal. Those need to be understood and removed/subtracted as well. In this situation, a suitable choice of statistical tools for the study of event-by-event fluctuations is really important.

## 3.1 $\Phi_{p_T}$ and $\sigma^2_{p_T,dyn}$

There are numerous observables which can be used to quantify $p_T$ fluctuations in high energy collisions. A natural one is the distribution of the average transverse

momentum of the events defined as:

$$M(p_T) = \frac{\sum_{i=1}^{N} p_{Ti}}{N}, \tag{3.1}$$

where $N$ is the multiplicity of accepted particles in a given event and $p_{Ti}$ is the transverse momentum of the i-th particle. The distribution of $M(p_T)$ is usually compared to the corresponding distribution obtained for mixed events in which the particles are independent from each other and follow the experimental inclusive spectra (mixed events are constructed such that the multiplicity distribution is the same as for the data). A difference between the two distributions signals the presence of dynamical fluctuations.

In the following, we briefly review quantities which have been proposed as measures for event-wise mean $p_T$ fluctuations and summarize notations used in this study.

The notations of various means and variances are defined as follows. With a measure $x$ of each particle, the mean of $x$ over particles within the acceptance in an event is defined as:

$$[x] \equiv \frac{\sum_{i=1}^{N} x_i}{N}, \tag{3.2}$$

where $i$ and $N$ indicate the particle index and the multiplicity, respectively.

With a measure defined in each event, $X$, the mean over all the events is defined as:

$$\langle X \rangle \equiv \frac{\sum_{j=1}^{n} w_j X_j}{n}, \tag{3.3}$$

where $j$ and $n$ indicate the event index and the number of events, respectively. The weighting factor for each event, $w_j$ is defined to be $N_j$ for $X = [x]$ (see below), and 1 otherwise.

The event-by-event variance of $X$ is defined as:

$$\langle \Delta X^2 \rangle \equiv \langle X^2 \rangle - \langle X \rangle^2. \tag{3.4}$$

The inclusive mean (the mean over all particles in all events) and variance of the measure $x$ of each particle are defined as:

$$\overline{x} \equiv \frac{\sum_{j=1}^{n} \sum_{i=1}^{N_j} x_i}{\sum_{j=1}^{n} N_j}, \tag{3.5}$$

and

$$\overline{\Delta x^2} \equiv \overline{x^2} - \overline{x}^2, \tag{3.6}$$

where $N_j$ represents $N$ in event $j$. The mean and the variance of $[x]$ are defined by replacing $X$ with $[x]$ in the above equations and including the event multiplicities as appropriate weighting factors:

$$\langle [x] \rangle \equiv \frac{\sum_{j=1}^{n} N_j \frac{\sum_{i=1}^{N_j} x_i}{N_j}}{n\langle N \rangle} = \overline{x} \tag{3.7}$$

and

$$\langle \Delta[x]^2 \rangle \equiv \frac{\sum_{j=1}^{n} N_j \frac{([x]-\langle [x] \rangle)^2}{N_j^2}}{n\langle N \rangle}. \tag{3.8}$$

This weighting procedure provides the most precise estimate of the variance of the parent distribution in case of finite mean multiplicity [35].

In the present event-by-event analysis, we search for dynamical mean $p_T$ fluctuations beyond those expected in a purely statistical scenario. Dynamical mean $[p_T]$ fluctuations would therefore result in an event-by-event distribution of M($p_T$) which is wider than that expected from the inclusive $p_T$ distribution and the finite event multiplicity. Measures for the mean $p_T$ fluctuations are constructed as a difference or a quadratic difference between the standard deviation of the $[p_T]$ distribution and the inclusive $p_T$ distribution normalized with the square-root of mean multiplicity.

In previous analyses, the measure $\Phi_{p_T}$ has been used to quantify non-statistical mean $p_T$ fluctuations, defined as [36]:

$$\Phi_{p_T} \equiv \sqrt{\frac{\langle Z^2 \rangle}{\langle N \rangle}} - \sqrt{\overline{z^2}}, \tag{3.9}$$

where $z$ and $Z$ are defined as $z \equiv p_T - \overline{p_T}$ for each particle, and $Z \equiv \sum_{i=1}^{M} z_i$ for each event, respectively. There is an approximate expression for $\Phi_{p_T}$ in terms of the variances of the event-wise M($p_T$) and the r.m.s. of the inclusive $[p_T]$ distributions [37]:

$$\Phi_{p_T} \cong \sqrt{\langle N \rangle}\sqrt{\langle \Delta[p_T]^2 \rangle} - \sqrt{\overline{\Delta p_T^2}}. \tag{3.10}$$

A different measure for dynamical mean $p_T$ fluctuation has been proposed in [37]:

$$\sigma^2_{p_T,dyn} \equiv \langle \Delta[p_T]^2 \rangle - \frac{\overline{\Delta p_T^2}}{\langle N \rangle}. \tag{3.11}$$

This expression provides a direct relation between the variance of the inclusive $[p_T]$ distribution, the mean multiplicity and the variance of the event-by-event mean $[p_T]$ distribution. In case of vanishing non-statistical fluctuations and correlations, $\sigma^2_{p_T,dyn}$ is equal to zero.

There is an important relation between the above two measures [37]:

$$\sigma^2_{p_T,dyn} \cong \frac{2\Phi_{p_T}\overline{\Delta p_T^2}}{\langle N \rangle}. \tag{3.12}$$

It has also been shown that $\sigma^2_{p_T,dyn}$ is the mean of covariances of all the possible pairs between two different particles [37]:

$$\sigma^2_{p_T,dyn} \cong \frac{1}{n_{events}} \sum_{k=1}^{n_{events}} \left[ \frac{1}{N_k(N_k-1)} \sum_{i \neq j}^{N_k} (p_{Ti} - \overline{p_T})(p_{Tj} - \overline{p_T}) \right]. \tag{3.13}$$

## 3.2 The average momentum correlator $\langle \overline{\Delta} p_{t,1} \overline{\Delta} p_{t,2} \rangle$

The second part of the equation 3.13, provides the main measure that is used in the present study. The **average momentum correlator** $\langle \overline{\Delta} p_{t,1} \overline{\Delta} p_{t,2} \rangle$ is defined as:

$$\langle \overline{\Delta} p_{t,1} \overline{\Delta} p_{t,2} \rangle \equiv \frac{1}{n_{events}} \sum_{k=1}^{n_{events}} \left[ \frac{1}{\frac{1}{2}N_k(N_k-1)} \sum_{i \neq j}^{N_k} (p_{Ti} - \overline{p_T})(p_{Tj} - \overline{p_T}) \right] \cong \sigma^2_{p_T,dyn} \tag{3.14}$$

where $\overline{p_T}$ is the inclusive mean $p_T$, $n_{events}$ is the number of analyzed events, $N_k$ is the number of particles from the event 'k', $p_{Ti}$ and $p_{Tj}$ are the transverse momentums of the $i^{th}$ and $j^{th}$ particle in an event, respectively.

The average momentum correlator is a covariance [38] and an integral of 2-body correlations [67]. Due to the central limit theorem [39], in a pure statistical distribution it equals zero in the absence of dynamical fluctuations and is defined to be positive for correlation and negative for anticorrelation. We define the sign of the fluctuation as the sign of the measure. It is also considered to be independent of random detection inefficiencies. The main advantage of that measure

is that it allows to select pairs by charge sign, as well as to make differential studies as a function of the angular pair separation, $\Delta\phi$, and of the separation in pseudo-rapidity, $\Delta\eta$.

The transverse momentum covariance $\langle\langle\delta p_{t_i}\delta p_{t_j}\rangle_{i\neq j}\rangle$ [38] is defined as:

$$\langle\langle\delta p_{t_i}\delta p_{t_j}\rangle_{i\neq j}\rangle \equiv \frac{\sum_{k=1}^{n_{events}}\left[\sum_{i\neq j}^{N_k}(p_{Ti}-\overline{p_T})(p_{Tj}-\overline{p_T})\right]}{\sum_{k=1}^{n_{events}}\frac{1}{2}N_k(N_k-1)} \tag{3.15}$$

The two aforementioned measures are approximately equal:

$$\langle\overline{\Delta}p_{t,1}\overline{\Delta}p_{t,2}\rangle \cong \langle\langle\delta p_{t_i}\delta p_{t_j}\rangle_{i\neq j}\rangle \tag{3.16}$$

In addition to the transverse momentum fluctuations given by the previous equation 3.14 for all charged particles, one can investigate the $p_T$ fluctuations of the negative and positive charges independently, as well as the cross correlation between them. For like-sign particles, the average momentum correlation is:

$$\langle\overline{\Delta}p_{t,1}^{\pm}\overline{\Delta}p_{t,2}^{\pm}\rangle \equiv \frac{1}{n_{events}}\sum_{k=1}^{n_{events}}\left[\frac{1}{\frac{1}{2}N_k^{\pm}(N_k^{\pm}-1)}\sum_{i\neq j}^{N_k^{\pm}}(p_{Ti}^{\pm}-\overline{p_T^{\pm}})(p_{Tj}^{\pm}-\overline{p_T^{\pm}})\right] \tag{3.17}$$

For the unlike-sign pairs we get:

$$\langle\overline{\Delta}p_{t,1}^{+}\overline{\Delta}p_{t,2}^{-}\rangle \equiv \frac{1}{n_{events}}\sum_{k=1}^{n_{events}}\left[\frac{1}{N_k^{+}N_k^{-}}\sum_{i,j}^{N_k^{+},N_k^{-}}(p_{Ti}^{+}-\overline{p_T^{+}})(p_{Tj}^{-}-\overline{p_T^{-}})\right] \tag{3.18}$$

## 3.3 The normalized dynamical fluctuation $\Sigma_{p_T}$

In order to account for a possible change of mean $p_T$ at different beam energies, we define a dimensionless measure, the "normalized dynamical fluctuation" $\Sigma_{p_T}$ [40], as:

$$\Sigma_{p_T} = \sigma_{p_T,dyn}/\overline{p_T} \equiv \mathrm{sgn}(\sigma^2_{p_T,dyn})\frac{\sqrt{|\sigma^2_{p_T,dyn}|}}{\overline{p_T}}. \tag{3.19}$$

where $\mathrm{sgn}(x) = 1$ if $x > 0$, $\mathrm{sgn}(x) = -1$ if $x < 0$, and $\mathrm{sgn}(x) = 0$ if $x = 0$.

The measure $\Sigma_{p_T}$ expresses the magnitude of non-statistical fluctuations in percent of the inclusive mean transverse momentum $\overline{p_T}$.

The best way for a quantitative determination of mean $p_T$ fluctuations is the use of a dimensionless measure. In addition, a comparison between different experiments should be possible. In this context $\Phi_{p_T}$ is neither dimensionless nor independent of the event multiplicity. This makes a comparison between experiments and to theory difficult because multiplicity depends on the acceptance window of the experiment and on beam energy. Since different contributions to the fluctuation signal have different multiplicity dependences, the multiplicity dependence of $\Phi_{p_T}$ is *a priori* unknown.

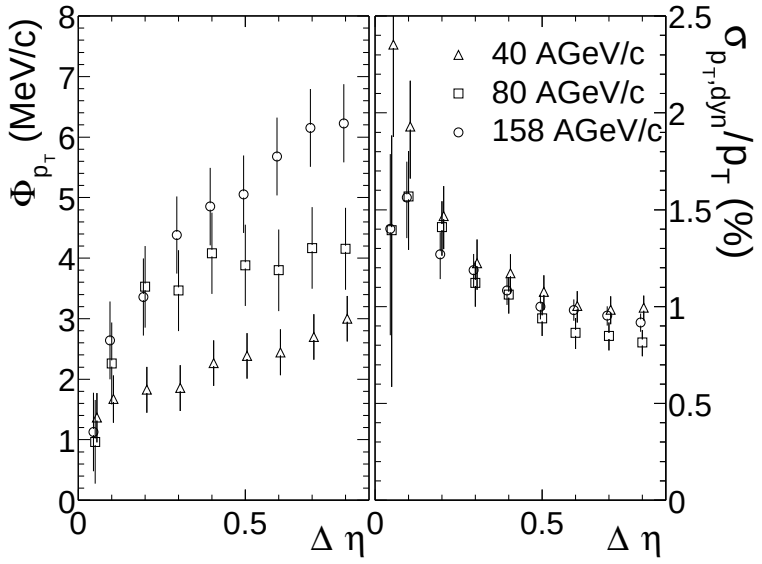


Figure 3.1: The $\Phi_{p_T}$ [MeV/c] (left panel), and $\sigma_{p_T,dyn}/\overline{p_T}$ [%] (right panel) at 40, 80, and 158 A·GeV/c in the 6.5 % most central events as a function of $\eta$ bin size $\Delta\eta$ with the $\eta$ center fixed to 2.45 [45].

Fig. 3.1 [45] shows $\Phi_{p_T}$ and $\sigma_{p_T,dyn}/\overline{p_T}$ as a function of $\eta$ bin size $\Delta\eta$ at 40, 80, and 158 A·GeV/c. The $\Phi_{p_T}$ increases as a function of $\Delta\eta$, while $\sigma_{p_T,dyn}/\overline{p_T}$ decreases at small $\Delta\eta$ and tends to saturate at $\Delta\eta \geq 0.5$. The $\sigma_{p_T,dyn}/\overline{p_T}$ roughly agrees among the three beam energies at all $\Delta\eta$ bins, while $\Phi_{p_T}$ varies among the beam beam energies, which can be understood due to the scaling with mean multiplicity shown in Eq. 3.12. This clearly shows $\sigma_{p_T,dyn}/\overline{p_T}$ ($=\Sigma_{p_T}$) is a universal measure independent of multiplicity within the acceptance.

## 3.4 $\Delta\sigma_{\langle p_T\rangle}$ and $F_{p_T}$

Another measure is $\Delta\sigma_{\langle p_T\rangle}$ [39], defined as:

$$\Delta\sigma_{\langle p_T\rangle} \equiv \sqrt{\langle N\rangle}\sigma_{\langle p_T\rangle} - \sigma_{p_T}, \tag{3.20}$$

where $\sigma_{\langle p_T\rangle}$ is the r.m.s. of the event-by-event $\langle p_T\rangle$ distribution, $\sigma_{p_T}$ is the r.m.s. of the inclusive(track-by-track) $p_T$ distribution. There is an approximation

$$\Phi_{p_T} \cong \Delta\sigma_{\langle p_T\rangle} \tag{3.21}$$

The last measure, introduced by Stephanov *et. al.* [35], is defined as follows:

$$F \equiv \frac{\langle N\rangle\sigma^2_{\langle p_T\rangle}}{\sigma^2_{p_T}}. \tag{3.22}$$

$F$ can be related to a 2-particle correlation function;

$$F = \frac{1}{\langle N\rangle}\sum_{p}^{N_{bin}}\sum_{k}^{N_{bin}}\langle\Delta n_p\Delta n_k\rangle\frac{(p_T - \overline{p_T})(k_T - \overline{k_T})}{\sigma^2_{p_T}}, \tag{3.23}$$

where $p$, $k$ are indices for a bin (e.g. $\eta$ bin).

$$F - 1 = \frac{1}{\langle N\rangle}\sum_{p\neq k}\langle\Delta n_p\Delta n_k\rangle'\frac{\Delta p_T\Delta k_T}{\sigma^2_{p_T}} \tag{3.24}$$

The relation between $F$ and $\Phi_{p_T}$ is as follows:

$$\Phi_{p_T} = \sigma_{p_T}(\sqrt{F} - 1) \tag{3.25}$$

## 3.5 Discussion

A quantitative event-by-event study requires an appropriate formalism which facilitates a comparison of results among different experiments and to theory. Unfortunately, most of the experiments use different measures for fluctuations. These measures have very different sensitivities to particular experimental conditions, such as track quality cuts, tracking efficiency and acceptance. In this sense, measures which are most closely related to single- and two-particle densities appear preferable since they are the least sensitive to trivial efficiency effects

[41]. In this case, it is mandatory that experiments provide all the information necessary for an approximative conversion of one measure into another.

In this work, the measures $\sigma^2_{p_T,dyn}$, $\Sigma_{p_T}$, and $\langle\overline{\Delta}p_{t,1}\overline{\Delta}p_{t,2}\rangle$ are used to study mean $p_T$ fluctuations.

When studying the centrality dependence, the following approximate relations can be used:

$$\langle N\rangle\sigma^2_{p_T,dyn} \propto F_{p_T} \propto \Phi_{p_T}. \tag{3.26}$$

Implying that particle production at SPS is approximately proportional to the number of participating nucleons, the multiplicity $\langle N\rangle$ can be replaced by the mean number of participating nucleons $\langle N_{part}\rangle$ which can be calculated much easier and does not depend on the acceptance.

# Chapter 4

# Previous Results on Event-by-Event Mean $p_T$ Fluctuations at SPS energies

## 4.1 Introduction

In this chapter, results obtained previously by the CERES collaboration from Pb-Au collisions at 40, 80, and 158 A·GeV/c [46] are presented.

Fig. 4.1 shows a comparison between event-by-event mean $p_T$ distributions obtained from real and mixed Pb-Au events at 40, 80, and 158 A·GeV/c. Both distributions exhibit very similar Gamma distribution shapes [47]. However, the ratio of real to mixed events in the tails of the distributions shows enhancement at extreme-$p_T$ regions. This is an evidence for the non-statistical fluctuations and wider distributions of real compared to statistical distributions. Their small difference demonstrates that dynamical fluctuations are small compared to statistical ones. Moreover, no distinct class of events with unusual fluctuations is observed.

The main objectives are to quantify magnitudes of the observed $p_T$ fluctuations, and to observe how the fluctuation pattern changes with increasing number of nucleons participating in a collision, i.e. with system size, and what is the collision energy dependence.

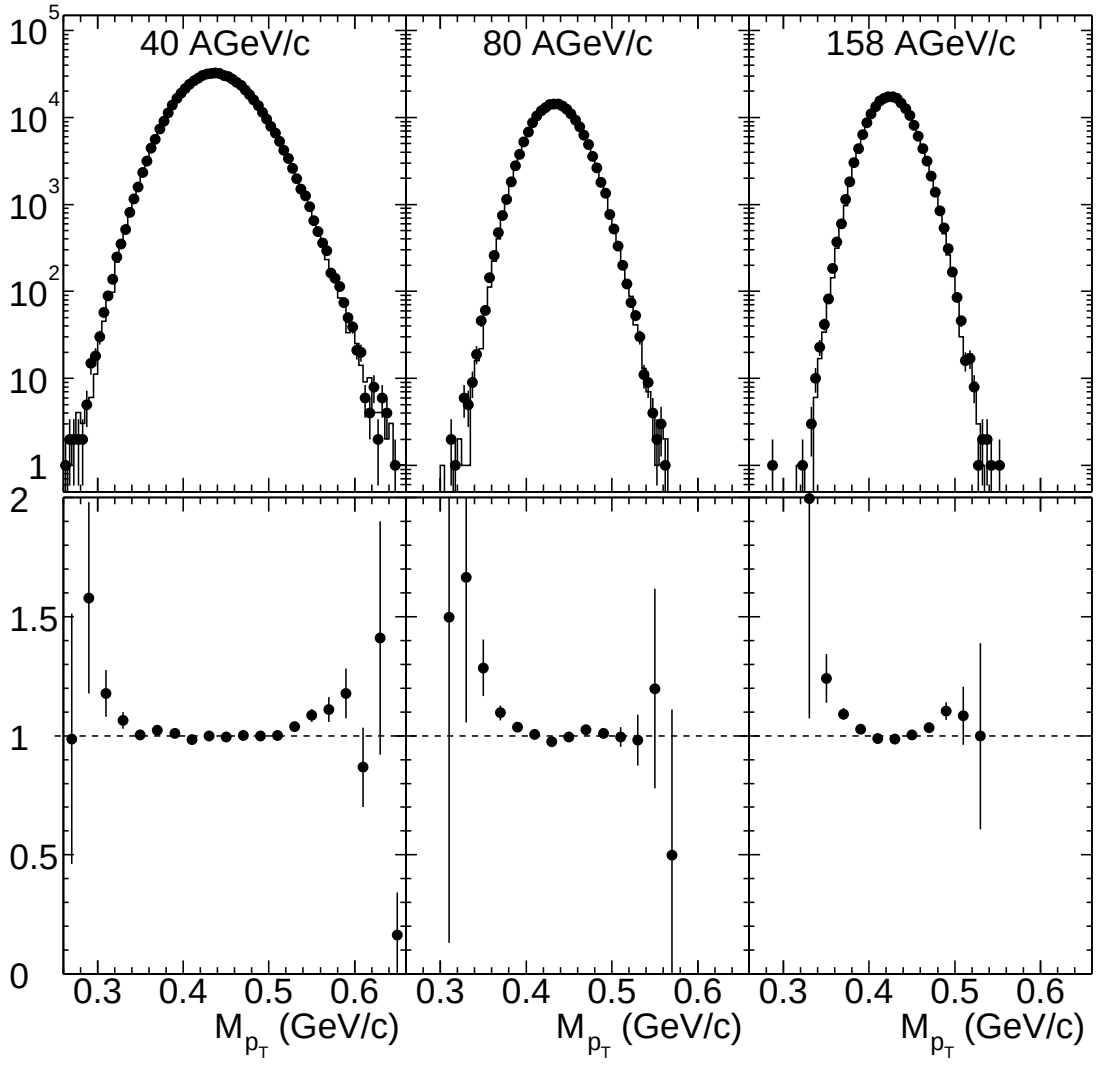


Figure 4.1: Top : event-by-event mean $p_T$ distributions for 40 (left), 80 (middle), and 158 A·GeV/c (right) data. Circles show real data, and solid lines show mixed events. Bottom: ratio of distributions from real events to those from mixed events for 40 (left), 80 (middle), and 158 A·GeV/c (right) data.

## 4.2 Beam energy dependence

The robust measure $\Sigma_{p_T}$ (see section 3.19) is used to investigate the collision energy dependence. As it was pointed out previously, the measure $\Sigma_{p_T}$ is dimensionless and specifies the dynamical contribution to event-by-event $M(p_T)$ fluctuations in fractions of $\overline{p_T}$. In the case of independent particle emission from single parent distribution, $\Sigma_{p_T}$ is zero.

The finite two-track separation of the TPC leads to a suppression of particle pairs with small momentum difference and consequently to a slight anti-correlation of particles in momentum space. In the case of CERES-TPC, the effect on $\Sigma_{p_T}$ is negligible [45], hence no correction has been applied. Positive correlations may arise due to quantum statistics, flow, jets and other *physics* effects which have also not been corrected for.

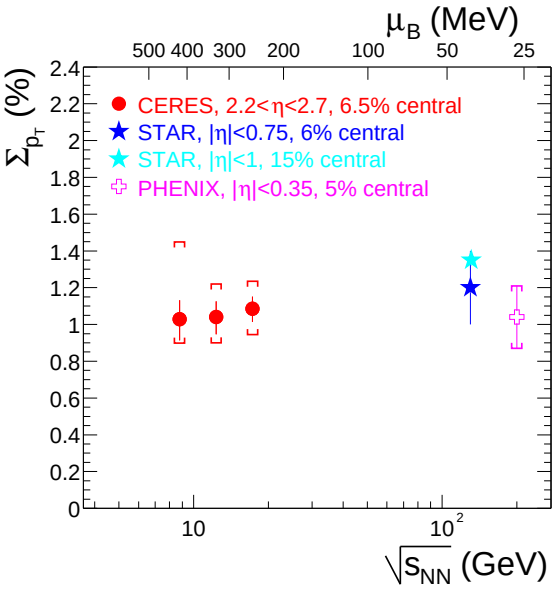


Figure 4.2: The normalized dynamical fluctuation, $\Sigma_{p_T}$ [%], as a function of nucleon-nucleon center-of-mass energy $\sqrt{s_{NN}}$ [GeV].

A compilation of the normalized dynamical fluctuation, $\Sigma_{p_T}$, measured at mid-rapidity and at different beam energies is shown in Fig. 4.2. The upper scale indicates the baryon chemical potential $\mu_B$ at chemical freeze-out, related to $\sqrt{s_{NN}}$ via a phenomenological parametrization given in [48]. The $\Sigma_{p_T}$ that are

measured by CERES at beam energy of 40, 80 and 158 A·GeV/c, in $2.2 < \eta < 2.9$ and $0.1 < p_T < 2$ GeV/c in 6.5 % cental events are compared to RHIC data at $\sqrt{s_{NN}} = 130$ GeV [49, 50] and 200 GeV [51].

The observed fluctuations at SPS and at RHIC are similarly about 1 %. The evolution of $\Sigma_{p_T}$ with beam energy looks smooth and does not show any indication of unusually large fluctuations at any beam energy.

Models predict enhanced mean $p_T$ fluctuations if the system has passed close to the critical point of the QCD phase diagram. At SPS energies and for the finite rapidity acceptance window of the CERES experiment, the fluctuations should reach values of about 2 %, i.e. more than two times larger than observed in the present data [35, 52] . However, no indication for a non-monotonic behaviour as function of the beam energy has been observed. This suggests that the critical point may not be located in the $\mu_B$ regime below 450 MeV.

## 4.3 Centrality dependence

As a reference for the centrality dependence of $\Sigma_{p_T}$, the measurements in hadron-hadron collisions are employed. In *p-p* interactions, particles are produced in a correlated way which leads to large non-statistical fluctuations. At the ISR, dynamical mean $p_T$ fluctuations have been measured in *p-p* reactions at $\sqrt{s_{NN}}$ = 30.8-63.0 GeV [53]. Independent of beam energy, a value of 12 % of $\overline{p_T}$ was observed for $\Sigma_{p_T}$. In $\alpha - \alpha$ reactions, the observed dynamical fluctuation is reduced to about 9 % of $\overline{p_T}$. If particle production in $\alpha - \alpha$ collisions acts like an independent superposition of *p-p* collisions, the fluctuations may scale with the multiplicity of produced particles:

$$\Sigma_{p_T}^{AA} = \Sigma_{p_T}^{pp} \left(\frac{\langle N_{pp} \rangle}{\langle N_{AA} \rangle}\right)^{1/2}. \tag{4.1}$$

Since the number of charged particles was found to scale close to linear with the number of participants $\langle N_{part} \rangle$ at SPS [54, 55, 56], the ratio of multiplicities in Eq. 4.1 can be replaced:

$$\Sigma_{p_T}^{AA} = \Sigma_{p_T}^{pp} (\langle N_{part} \rangle)^{-1/2}. \tag{4.2}$$

As demonstrated in Fig. 4.3 [57], the data agree with this extrapolation for very peripheral and central events. In contast, a pronounced deviation is observed

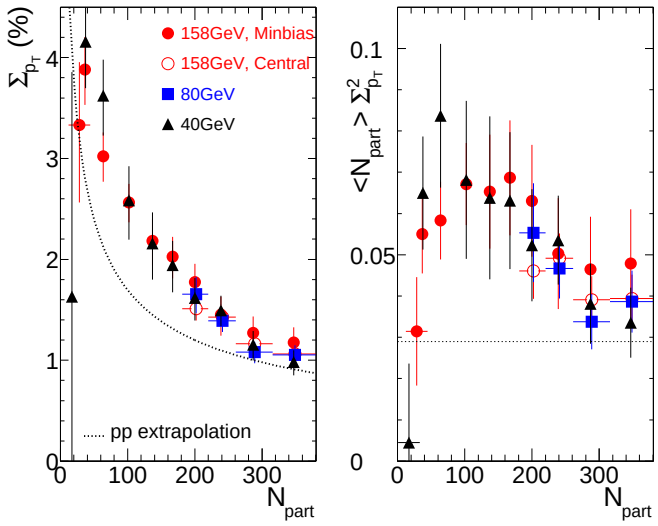


Figure 4.3: Centrality dependence of $\Sigma_{p_T}$ at 40, 80 and 158 A·GeV/c [57]

in semi-peripheral events. In the right panel of Fig. 4.3, the product $\langle N_{part}\rangle\Sigma^2_{p_T}$ is plotted as function of $\langle N_{part}\rangle$. In this representation, the $p$-$p$ extrapolation becomes a constant (=0.03), while the data exhibit a broad maximum around $N_{part} = 120$. This observation is in qualitative agreement with previous findings at SPS and RHIC. Other experiments like NA49, PHENIX and STAR [50, 51, 58, 59] also observe $M(p_T)$ fluctuations which are significantly increased over the $p$-$p$ extrapolation in semi-central events. PHENIX attributed the non-monotonic centrality dependence of the measure $F_{p_T}$ [51] to jet production in peripheral events, combined with jet suppression in more central events, causing a decrease of fluctuations. Other intepretations were given in terms of thermalization effects [60, 61], or in the framework of a string percolation model [62, 63].

## 4.4 Conclusions

The existence of non-statistical event-by-event fluctuations of the mean transverse momentum M($p_T$) at SPS and RHIC is by now well established. However, these dynamical fluctuations are small in central collisions, typically about 1 % of the

inclusive mean transverse momentum $\overline{p_T}$ and only weakly depend on $\sqrt{s_{NN}}$. In particular, no indication for a non-monotonic beam energy dependence has been found so far. The $p_T$ fluctuations also violate the trivial *1/N* scaling expected for nuclear collisions consisting of independent nucleon-nucleon interactions.

Despite the absence of a 'smoking gun' signature for the phase transition or the critical point, the systematic study of M($p_T$) fluctuations gives valuable insight into the particle production mechanism and the dynamic evolution of the system which cannot be extracted from inclusive distributions.

Although the mean $p_T$ fluctuations are not as large as anticipated, there remains the possibility that the observed fluctuations are reduced from their expected value due to some final thermal effects, or because only a small fraction of the system actually produces a QGP. A 'differential', scale-dependent analysis of M($p_T$) fluctuations is an essential tool that could shed light on their origin, providing more information.

# Chapter 5

# The CERES Experiment and the Data Analysis

## 5.1 The CERES Experiment

The CERES/NA45 experiment is optimized for di-electron measurements in proton and ion induced collisions at CERN-SPS [27, 28]. The spectrometer covers a broad range of $p_T$ close to midrapidity. Until 1996 the experiment consisted of two Ring Imaging Cherenkov detectors (RICH's) for electron identification, two silicon radial drift detectors (SDD's), and a pad chamber. A superconducting magnet (solenoid) between the RICHes provided a deflection field for the determination of the particle's charge and momentum. The silicon detectors together with the pad chamber were used as tracking devices. With this setup CERES measured a significant enhancement of low-mass $e^+e^-$ pairs in heavy ion collisions compared to contributions from hadronic decays, extrapolated from nucleon-nucleon collisions. In 1998 the spectrometer was upgraded by a tracking detector downstream of the existing setup, a cylindrical Time Projection Chamber (TPC) with radial drift field, which replaced the pad chamber in order to improve the di-electron invariant mass resolution [29]. The addition allowed CERES to serve as a hadron spectrometer.

All subdetectors have a common acceptance in the polar angle range of $8° < \theta < 15°$ at full azimuth, corresponding to a pseudorapidity acceptance of $2.1 < \eta < 2.65$. Fig. 5.1 shows a sketch of the setup.

In this analysis, only the two SDD's and the TPC were used for charged particle track reconstruction. The SDD's are located about 12 cm downstream of the target system. Each SDD has uniform drift field in the radial direction, with 360 anodes at the out-most radial position arranged azimuthally in 1° pitch. The TPC is located at 3.8 m downstream of the target system. In the TPC, the ionization electrons drift outward in the radial direction, with a drift field changing as $\sim 1/r$. Electron signals are detected in the Multi-Wire Proportional Chambers (MWPC's) at the outer radial position [29]. The magnetic field formed by two opposite-polarity solenoidal coils, which are placed around the TPC, deflects charged particle trajectories in the $\phi$ direction. The position resolutions are about 40 $\mu$m both in $r$ and $r\phi$ directions in the cylindrical coordinate system. The momentum resolution of the spectrometer reached after the final calibration is

$$\frac{\Delta p}{p} = 2\% \oplus 1\% \cdot p/\mathrm{GeV} \tag{5.1}$$

both from residuals of hits with respect to fitted tracks, and from invariant mass of $\Lambda$ and $K^0_s$. Such resolution results in $\frac{\Delta m}{m} = 0.038$ for the $\phi$ meson in the $e^+e^-$ channel. Particle identification is possible to a certain degree using the energy loss in the TPC gas with $\frac{\Delta(dE/dx)}{(dE/dx)} = 0.10$ [30]. The following sections of this chapter describe the main features of all detectors.

### 5.1.1 Target Area, Trigger and the Two Silicon Drift Detectors

The target system used during the beam-time 2000 (158 A·GeV/c Pb-beam period) consists of thirteen 25-$\mu$m thick Au discs, separated by 2 mm in beam direction, with a total thickness of 1.33% of a hadronic interaction length. The distance between the discs was chosen such that particles coming from a collision in a given target disc and falling into the spectrometer acceptance do not hit any other of the discs. This helps to minimize the conversion of $\gamma$'s into $e^+e^-$ -pairs which is essential for the analysis of electron pairs.

To start the read-out sequence of the detectors the occurence of a collision has to be detected. This is done with a system of beam/trigger detectors, shown in Fig. 5.2 in a simplified view. The beam counters BC1 to BC3 are used to

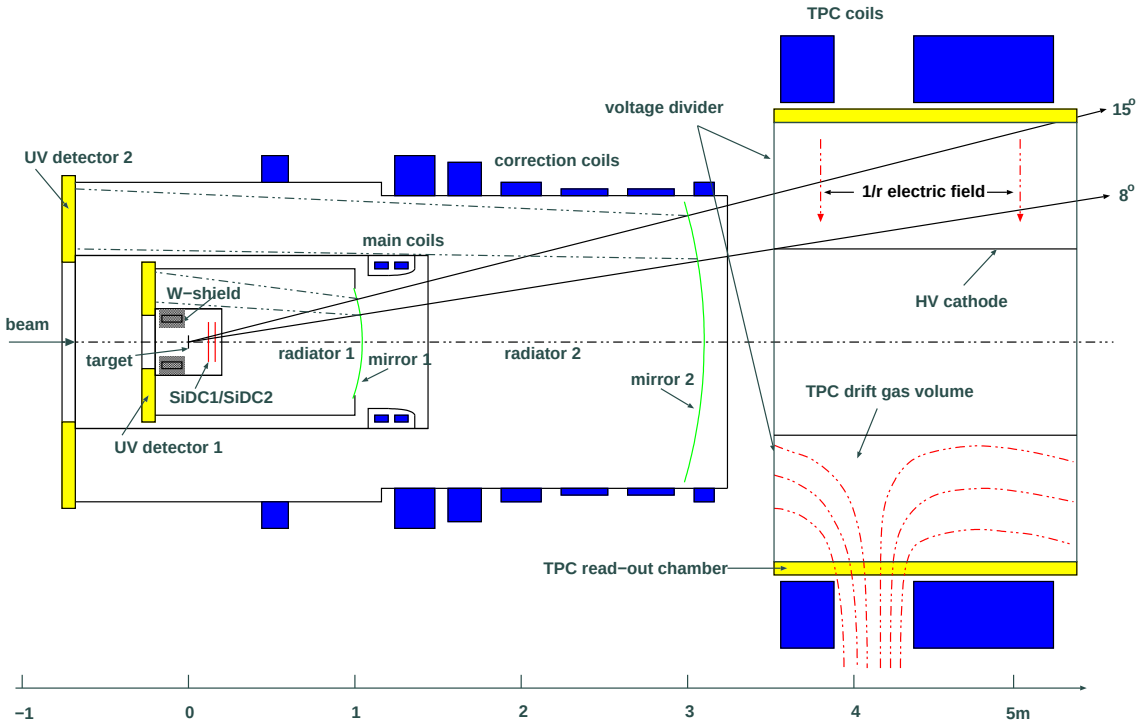


Figure 5.1: Schematic view CERES spectrometer.

detect collisions between projectile and target nuclei. These detectors are gas Cherenkov-counters with air as radiator, located on the beam-line. The beam trigger (BEAM) is defined by the coincidence of two beam counters (BC1 and BC2) located in front of the target, and the minimum bias trigger (MINB) is defined as BEAM and no signal in the beam counter (BC3) located after the target ($T_{MINB}$ = BC1×BC2×$\overline{BC3}$). The charged particle multiplicity is often used as a measure for the centrality of the collision. The MC or the MD detector can be used to select events with a certain multiplicity. These detectors are scintillation detectors and their output signal is approximately proportional to the number of ionizing particles passing through them. The central collision trigger is defined as CENT=MINB×MC.

The veto detectors VW and VC are both plastic scintillators. They can be used to discard interactions which happened before the target.

The silicon drift detectors(SDD's) are placed approximately 10 cm behind the target. Both detectors are realized on 4 inch silicon wafers with a thickness of

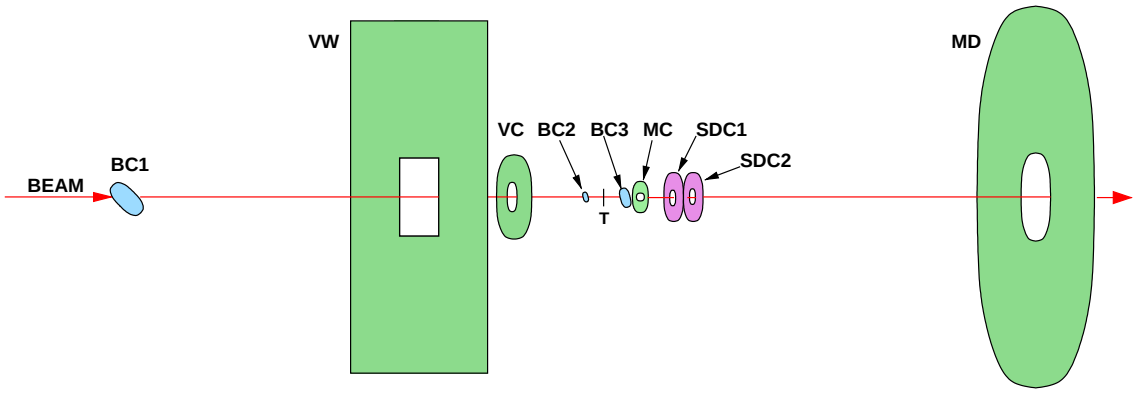


Figure 5.2: Schematic view of the target region with the trigger detectors.

280 $\mu$m. The sensitive area covers the region between the radii 4.5 mm and 42 mm with full azimuthal acceptance. They form a vertex telescope, which is a central part of the event and track reconstruction. These detectors provide a very precise reconstruction of an interaction vertex, a measurement of energy loss and coordinates of hundreds of charged particles with high spatial resolution and interaction rate, a track segment reconstruction before the magnetic field. The principle of operation, as well as details about the silicon drift detectors used in CERES and their performance, can be found in [32].

### 5.1.2 The RICH Detectors

Two Ring Imaging Cherenkov counters (RICH) are used to measure the velocity of the particle and their trajectory. If the momentum of the particle is known the mass can be determined. These detectors are invented by Seguinot and Ypsilantis [31] and rely on the position sensitive measurement of the emitted Cherenkov light. Inside a radiator Cherenkov-light is emitted under a constant angle $\theta_C$ with respect to the trajectory of the charged particle.

A ring imaging Cherenkov detector is schematically shown in Fig. 5.3. A spherical mirror reflects the emitted Cherenkov photons into ring images at the focal plane of the mirror. The diameter of these rings then corresponds to a certain Cherenkov angle and thus to the velocity of the particle. Both, the ring radius and the number of Cherenkov photons, depend on particle momentum and mass. Knowing the particle momentum, such detector can be used for particle identi-

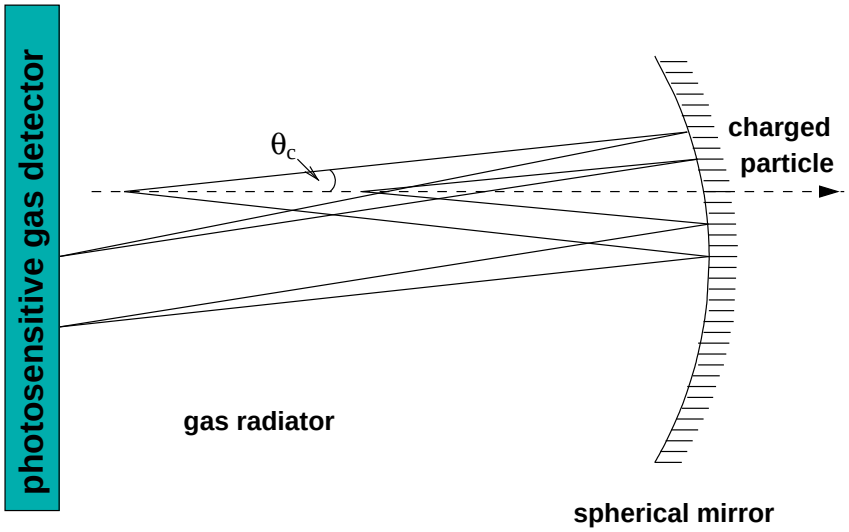


Figure 5.3: Schematic view of a RICH detector with a spherical mirror. The particle enters from the left, the emitted Cherenkov photons are reflected backward into a photon detector.

fication, or the other way around, knowing the particle mass, we can measure its momentum. The RICH detectors in the CERES spectrometer operate with $CH_4$ at atmospheric pressure as radiator gas. The threshold for light emission is thereby fixed to $\gamma_{th} = 32$. Practically all electrons produce light at the asymptotic angle whereas most hadrons, except pions with a momentum of more than 4.5 GeV, produce no signal at all. The detector is therefore practically hadron blind, which is very important for the dilepton measurement and also offers an excellent tool to study high-$p_T$ pions. The UV detectors used for the position sensitive measurement of the photons are gas counters with a gas composition of 94% helium and 6% methane. They are located at the focal plane of the mirrors.

### 5.1.3 The Time Projection Chamber

In 1998, the spectrometer was upgraded by an additional tracking detector, a **T**ime **P**rojection **C**hamber (TPC) with radial drift field, which replaced the pad chamber. The aim of the upgrade was to achieve the mass resolution of $\frac{\Delta m}{m} =$ 2% at m$\sim$1 GeV which would allow a precise spectroscopy of $\rho/\omega$ and $\phi$ vector mesons. The CERES TPC (shown in a perspective view in Fig. 5.4) is a cylin-

drical drift chamber filled with $Ne/CO_2$ gas mixture in ratio 80/20. This composition was chosen after optimization on diffusion, multiple scattering, Lorentz angle, primary ionization and drift velocity. The sensitive volume is about 9 $m^3$ and the length 2 m. It has 16 readout chambers with segmented pad-readout placed in a polygonal structure. Along the beam axis, the TPC is divided into 20 planes, each with $16 \times 48 = 768$ readout channels on the circumference. In total, 15360 individual channels with 256 time samples each can be read out, allowing a three-dimensional reconstruction of particle tracks. The electric field is approximately radial and is defined by the inner electrode, which is an aluminum cylinder at a potential of -30 kV, and the cathode wires of the readout chambers at ground potential. The avalanche produced close to the anode wires induces a signal in the chevron-type cathode pads [29].

The magnetic field in the sensitive detection volume is generated by two warm coils with current flowing in opposite directions. The radial component of this field is maximal between the two coils and the deflection of charged particles is mainly in azimuthal direction.

### Principle of Operation

The Time Projection Chamber [33] is an essentially three-dimensional tracking detector capable of providing information on many points of a particle track along with information on the specific energy loss, $dE/dx$, of the particle.

A charged particle produces electron ion pairs along its path through the detector. The electrons drift in the electric field towards a plane of proportional wires close to the pad plane. At distances of a few wire diameters the electron starts an avalanche process which creates free charges. Because the electrons are created very close to the wire they are captured by it and neutralized in a very short time. The movement of the much slower ions is responsible for the creation of the induced signal which is detected by the readout electronics. Moving charges lead to an induced current on the pads. This current is detected and recorded with the help of charge sensitive amplifiers attached to each pad. The measurement of the time between the start of the drift (which is essentially the time of the collision between a projectile and a target nucleus) and the arrival of the charge cloud at the wires combined with the knowledge of the drift velocity

enables the reconstruction of the radial coordinate of the tracks. The other two spatial coordinates are determined by the location of the pad. Due to the chevron shape of the pads the charge cloud is shared between adjacent pads. This allows for a precise reconstruction of the charge centroid in the azimuthal direction. Since the collected charge is proportional to the energy loss of the particle, the signal amplitudes from the anode also provide information on the $dE/dx$ of the particle. If the momentum of the particle is known from the curvature of its trajectory in the magnetic field, for example, then this information can be used to identify the particle.

Details about the TPC used in CERES as well as the readout system with the

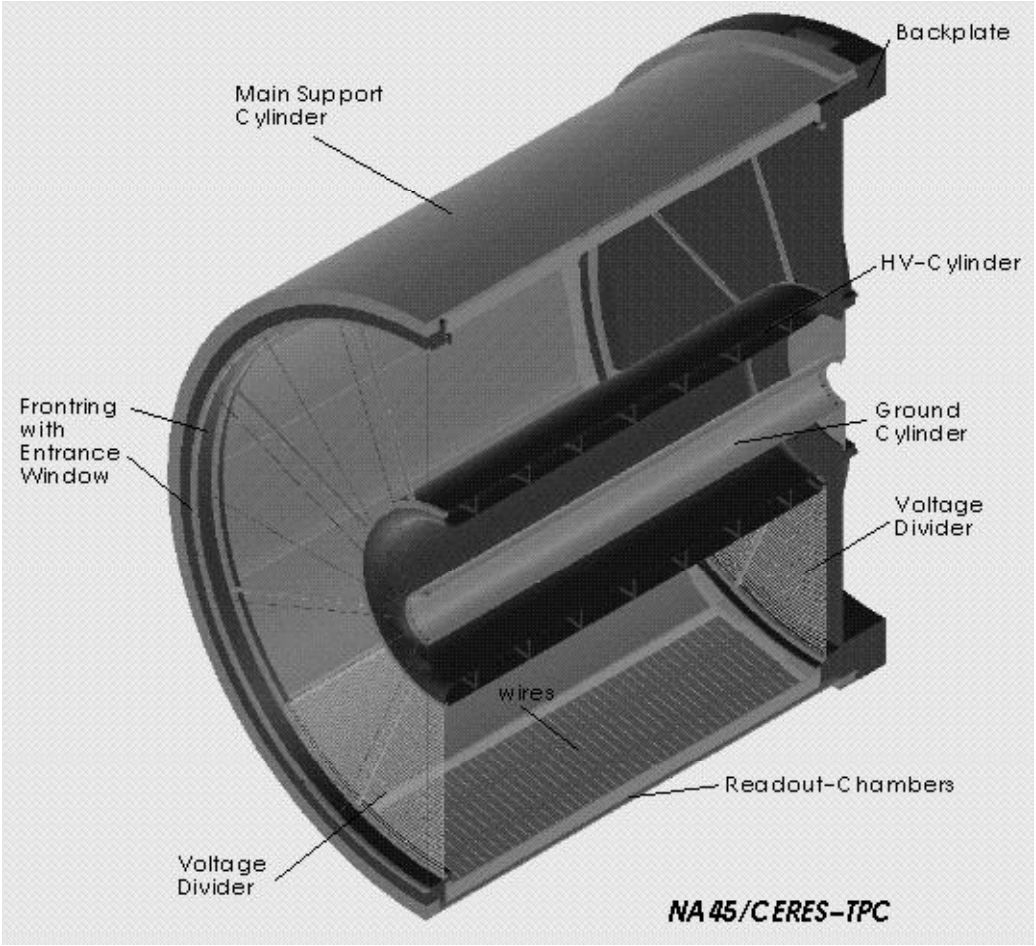


Figure 5.4: Perspective view of the TPC.

front-end, control and back-end electronics, can be found in [34].

## 5.2 Data Analysis

In the framework of this thesis, data samples of Pb-Au collisions taken at beam energy of 158 AGeV/c at the CERN SPS have been analyzed. A typical Pb beam intensity was $1 \times 10^6$ particles per burst. About 30 million Pb+Au collisions at 158 AGeV/c having a centrality of the upper 8 % of the total geometric cross section, and 3 million of 20 % have been collected during the beam period of the year 2000. In this analysis, we use 2 SDD's and a TPC for charged particle track reconstruction. The data taking rate in 2000 was $300 \sim 500$ events/burst.

### 5.2.1 Event Selection

The following event selection cuts were applied to exclude two superimposed Pb-Au collisions (pile-up events) or a collision of Pb-beam with non-target nucleus, which could have very different multiplicity and $p_T$ distributions compared to a single Pb+Au collision and could change magnitude of event-by-event fluctuations.

- Rejection of events with the number of TPC tracks less than 30 (defined below) to reject non-target interactions.
- Before- and after-protection cuts. In the trigger logic, a minimum time separation to another beam particle with respect to the triggered beam particle was required. It was set to $\pm$ 2 $\mu$s at 158 AGeV/c.
- Requirement of dE/dx of 2 beam counters (BC1, BC2) to be within $\pm 4\sigma$ from the peak values.

### 5.2.2 Centrality Determination

The collision centrality was determined via the charged particle multiplicity around midrapidity $y_{\rm beam}/2$=2.91. Two variables, the amplitude of the Multiplicity Counter (MC) (single scintillator covering 2.3$<\eta<$3.4) and the track

multiplicity in the TPC (2.1< $\eta$ <2.8), were alternatively used as the centrality measure (Fig. 5.5). Knowing the DAQ dead time factor (which describes the loss of events due to a busy DAQ) and the target thickness, and assuming that all beam particles were hitting the target, the event counts can be translated to the cross section for collisions with a given multiplicity. The integrated cross section, divided by the geometrical cross section $\sigma_G = 6.94$ barn, is shown as the additional axis in Fig. 5.5.

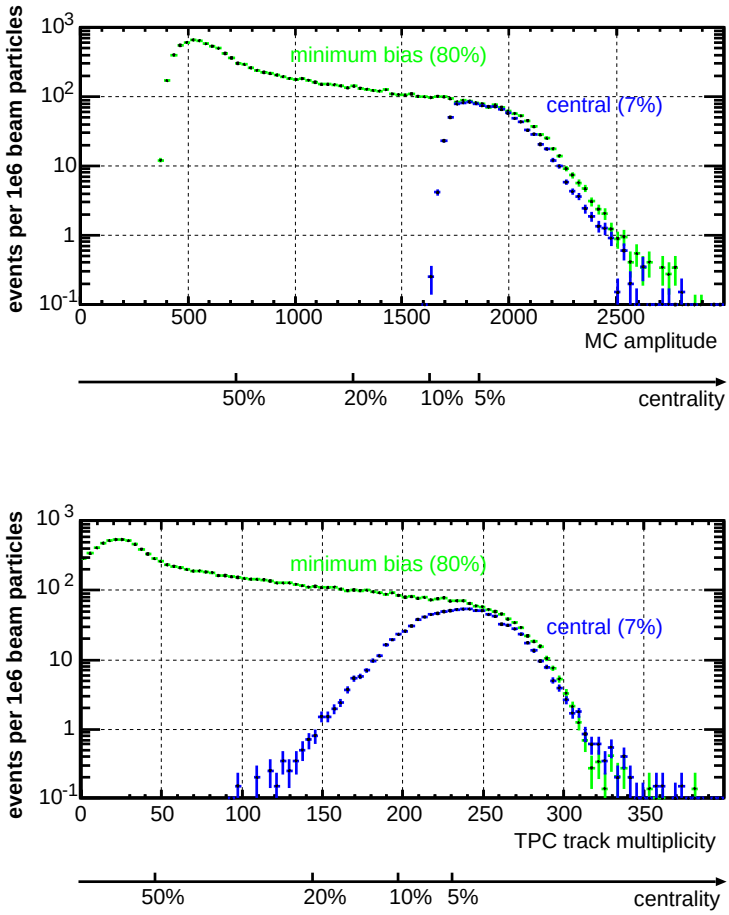


Figure 5.5: Distributions of the pulse height of the MC scintillator detector (top) and the TPC track multiplicity (bottom) used for centrality determination. The MC detector was used in the trigger. The distributions shown are before the run-by-run correction.

The centrality calibration of the CERES' 2000 data was done in two steps. First, a low beam-intensity minimum bias run is used to find the relation between the MC counter amplitude and the centrality. Second, the run-by-run variations

of the MC amplitude are corrected. Details can be found in [64].

In the present analysis we have applied an offline centrality selection of the upper 50 % of the total geometric cross section. The corresponding mean number of participating nucleons $\langle N_{part} \rangle$ and mean number of nucleon-nucleon collisions $\langle N_{coll} \rangle$ was derived from a geometric nuclear overlap model using $b = \sqrt{\sigma/\pi}$ and resulting, with $\sigma_{NN} = 30$ mb, in a total cross section of $\sigma_G = 6.94$ b [66]. Our classification of central events comprises the 8 % most central fraction of the total geometric cross section. For the centrality dependent studies we have subdivided our sample into five centrality classes (see Table 5.1).

| $\sigma/\sigma_{geo}$ [%] | $0-8$ | $10-20$ | $20-30$ | $30-40$ | $40-50$ |
|---|---|---|---|---|---|
| $\langle N_{part} \rangle$ | 328 | 221 | 153 | 102 | 64 |
| $\langle N_{coll} \rangle$ | 754 | 454 | 280 | 163 | 88 |

Table 5.1: Definition of centrality classes

### 5.2.3 Track Selection

A TPC track is reconstructed as an array of TPC hits on subsequent TPC $z-$planes, where the initial track-seed vector is required to point to the vertex. Depending on the polar angle, a TPC track consists of up to 20 hits. An initial track seed is reconstructed in middle planes, and it is extended to outer planes. In $\rho - z$ plane in the cylindrical coordinate system, hits are required to be on a straight line originating from the main vertex. In $\phi - z$ plane, a hit position on a plane is predicted from the projection of a local vector with previously found planes. Momentum is calculated as a fit parameter of hit positions of a track in the $r\phi - z$ plane to a track template which is generated with a Monte Carlo simulation. The vertex is reconstructed from all SDD1 hits and SDD2 hits, whose position resolution is about 6 $\mu$m. A SDD-track is required to have a SDD1 hit and a SDD2 hit which are on a straight line passing through the vertex. Association of a TPC track with a SDD track is done using the projections of the 2

tracks on the spherical surface of the RICH2 mirror where the multiple scattering is most probable. This inclusion of SDD track information leads to a powerful rejection of non-vertex tracks, if only TPC tracks with a match to the SDD are used in the analysis. The matching window is set to 10 mrad in a calibrated function of both $\theta$ and $\phi$, respectively.

In addition, a number of fiducial and quality cuts have been applied to provide stable tracking conditions and to reject tracks from secondary particles:

- The pseudo-rapidity cut of $2.2 < \eta < 2.7$, which corresponds to full-length TPC track acceptance, is applied in the mean $p_T$ fluctuations analysis to keep high momentum resolutions.

- The transverse momentum cut is defined as $0.1 < p_T < 1.5$ GeV/c for $p_T$ fluctuation analysis to keep high momentum resolutions. The minimum $p_T$ cut is set to exclude soft tracks with low efficiency and large contamination from non-vertex tracks. The maximum $p_T$ cut is necessary to suppress high momentum tracks which would dominate the calculation of the mean momentum and for which the momentum resolution is poor.

- The minimum number of fitted hits per track is 12 in the full-length TPC track acceptance.

- To suppress secondary particles it is required that the back-extrapolation of the particle trajectory into the target plane, given by $r_0$, misses the interaction point by no more than 10 cm in transverse direction. More technical information about the tracking in the CERES TPC can be found in [65].

Fig. 5.6 shows the inclusive $p_T$ distribution, the $\eta$ distribution, as well as those of the number of fitted hits in the TPC and $r_0$.

The results shown in the following chapter refer to *accepted* particles , i.e., particles that are accepted by the detector and pass all kinematic cuts and track selection criteria.

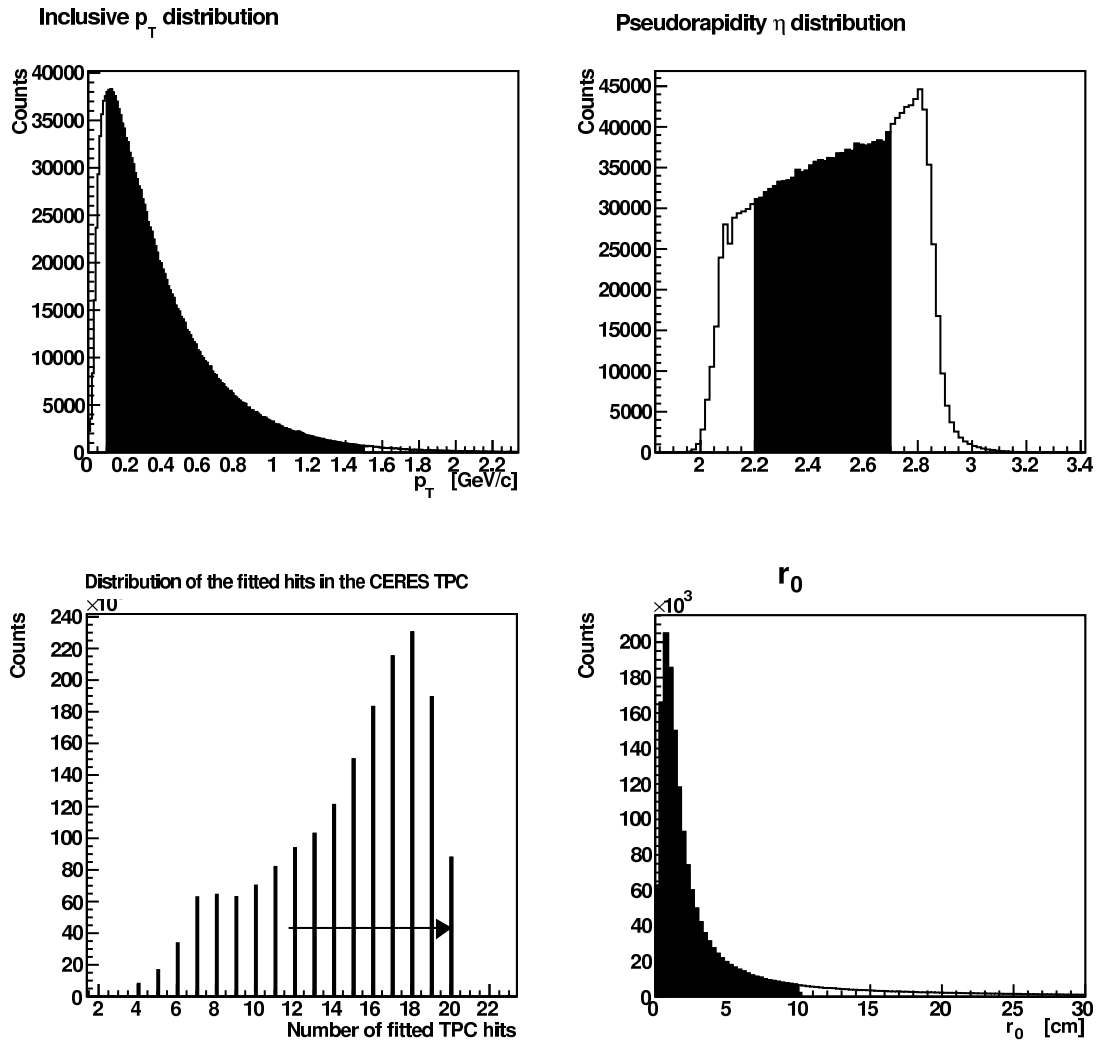


Figure 5.6: Distributions of $p_T$, $\eta$, number of fitted hits in the TPC and $r_0$.

# Chapter 6

# Scale dependence of Mean Transverse Momentum Fluctuations in $\Delta\eta$-$\Delta\phi$ space

Significant non-statistical event-by-event fluctuations and a characteristic centrality dependence have been observed over a wide range of beam energies. These results have been discussed in the context of QGP formation and the possibility to observe the QCD critical point.

It is important to note, that observation of a large magnitude of fluctuations would not by itself constitute the signal of the critical point. Since fluctations were characterized so far by one single number, it was difficult to estimate the many possible contributions to them.

Taking into account the high available statistics offered by the CERES experiment combined with the full azimuthal acceptance, we perform a differential study of mean $p_T$ fluctuations. Here, we present recent results of our analysis of data from the CERES collaboration on event-by-event fluctuations of the mean transverse momentum in Pb-Au collisions at 158 AGeV/c, obtained with a sample of about 10 million central events. For the first time at SPS energy, the charge-dependent mean $p_T$ fluctuations have been analyzed as a function of the angular pair separation, $\Delta\phi$, and of the separation in pseudorapidity, $\Delta\eta$. Apart from (expected) HBT correlations the data show a significant dependence on $\Delta\eta$ and $\Delta\phi$ that will be studied to shed light on their origin.

## 6.1 Inclusive results

Ten million central events are analyzed after all the quality cuts that are described in the previous chapter.

The resulting average momentum correlator $\langle \overline{\Delta} p_{t,1} \overline{\Delta} p_{t,2} \rangle$, the normalized dynamical fluctuation $\Sigma_{p_T}$, the $\sigma^2_{p_T,dyn}$, the mean multiplicity $\langle N_{part} \rangle$, and the inclusive mean transverse momentum $\overline{p_T}$ for all pairs, as well as for different charge combinations are given in Table 6.1. The fluctuations are not corrected for two-track resolution and HBT/Coulomb correlations.

For the calculation of $\Sigma_{p_T}$, the $\sigma^2_{p_T,dyn}$ was used, via the equations 3.11 and 3.19. The average momentum correlator $\langle \overline{\Delta} p_{t,1} \overline{\Delta} p_{t,2} \rangle$ is calculated using the formula 3.14.

We find that the expected approximation $\langle \overline{\Delta} p_{t,1} \overline{\Delta} p_{t,2} \rangle \cong \sigma^2_{p_T,dyn}$ holds very well. In addition, the measured $\Sigma_{p_T}$ is about 1 % and agrees with the previous measurements of finite non-statistical fluctuations of transverse momentum that are reported in chapter 4.2. Since $\langle \overline{\Delta} p_{t,1} \overline{\Delta} p_{t,2} \rangle$ and $\Sigma_{p_T}$ are global observables, a small value of them does not neccessarily imply the absence of any strong correlation. It is also possible that contributions of two effects just cancel out each other.

After these consistency checks which verify the measures we use to study mean $p_T$ fluctuations, we perform a 'differential' scale-dependent analysis in order to re-evaluate our need for more sensitivity.

| Beam energy [A·GeV/c] | 158 |
|---|---|
| All pairs | |
| $\langle\overline{\Delta}p_{t,1}\overline{\Delta}p_{t,2}\rangle[MeV^2]$ | $22.71 \pm 0.32$ |
| $\Sigma_{p_T}$ [%] | $1.04 \pm 0.01$ |
| $\sigma^2_{p_T,dyn}[MeV^2]$ | $21.98 \pm 0.44$ |
| $n$ | 10003672 |
| $\langle N\rangle$ | $154.83 \pm 0.01$ |
| $\overline{p_T}$ [MeV/c] | $449.82 \pm 0.01$ |
| Positive pairs | |
| $\langle\overline{\Delta}p_{t,1}\overline{\Delta}p_{t,2}\rangle[MeV^2]$ | $21.59 \pm 0.63$ |
| $\sigma^2_{p_T,dyn}[MeV^2]$ | $20.65 \pm 0.61$ |
| $n$ | 9009425 |
| $\langle N\rangle$ | $84.21 \pm 0.01$ |
| $\overline{p_T}$ [MeV/c] | $479.78 \pm 0.01$ |
| Negative pairs | |
| $\langle\overline{\Delta}p_{t,1}\overline{\Delta}p_{t,2}\rangle[MeV^2]$ | $26.63 \pm 0.61$ |
| $\sigma^2_{p_T,dyn}[MeV^2]$ | $26.16 \pm 0.54$ |
| $n$ | 9009425 |
| $\langle N\rangle$ | $70.63 \pm 0.01$ |
| $\overline{p_T}$ [MeV/c] | $414.10 \pm 0.01$ |
| Unlike-sign pairs | |
| $\langle\overline{\Delta}p_{t,1}\overline{\Delta}p_{t,2}\rangle[MeV^2]$ | $24.71 \pm 0.43$ |
| $n$ | 9009425 |

Table 6.1: Summary of mean $p_T$ fluctuations for all pairs and different charge combinations at $0.1 < p_T < 1.5$ GeV/c, $2.2 < \eta < 2.7$ and full $\phi$ acceptance at 158 A·GeV/c in the 8 % most central events. Errors are statistical only. The fluctuations are not corrected for two-track resolution and HBT/Coulomb correlations.

## 6.2 Differential analysis

A central goal in Event-by-Event analysis has been to develop global comparison measures sensitive to excess variance which might signal residual correlations due to incomplete equilibration − possibly structure remaining from a phase transition. The present treatment makes it clear that global-variables analysis based on average values (integrals) is rather limited in its sensitivity, interpretability and power to discriminate among various correlation sources. Thus, there is a need to resolve these global measures in a way that could provide us more information related to the 'origin' of the observed fluctuations.

It was pointed out in the previous chapter, that the pseudo-rapidity of accepted particles is restricted to the interval $2.2 < \eta < 2.7$ and there is a full azimuthal acceptance.

Particle pairs $(i, j)$ can be separated on axial *difference variables* as follows:

$$0 \leq \Delta\phi = |\phi_i - \phi_j| \leq 180^\circ \tag{6.1}$$

and:

$$0 \leq \Delta\eta = |\eta_i - \eta_j| \leq 0.5 \tag{6.2}$$

Where $i$ and $j$ are the particle indices.

The bin size in $\Delta\phi$ should be approximately equal to that in $\Delta\eta$, in terms of solid angle. In our case, this means:

Our $\theta$ acceptance is about 120 mrad, corresponding to $\Delta\eta$ about 0.5. Making a bin size of $\Delta\eta$=0.1, this corresponds to about 24 mrad. At this $\theta$, the Jacobian is about 5 ($\sim 1/sin\theta$), leading to a $\Delta\phi$ of 120 mrad, or 7 degrees.

Therefore, we divide the $\Delta\eta$-$\Delta\phi$ space into 120 bins in total. 5 bins in $\Delta\eta$ and 24 in $\Delta\phi$ corresponding to an angle of 7.5 degrees.

### 6.2.1 Mixed event analysis

As a baseline of the statistical distribution, and also for a consistency check of our analysis procedure for statistical distributions, we construct mixed events. To ensure that there is no correlation between any pair of particles, we pick up every track randomly from a different real event, using exactly the same

multiplicity distributions as the real data. The $\langle\overline{\Delta}p_{t,1}\overline{\Delta}p_{t,2}\rangle$ value calculated for the sample of mixed events was consistent with zero. The obtained average value is $\langle\overline{\Delta}p_{t,1}\overline{\Delta}p_{t,2}\rangle_{mixed} = -0.049 \pm 0.314\ MeV^2$.

In the second step, for each bin in $\Delta\eta$-$\Delta\phi$ space, we calculate the $\langle\overline{\Delta}p_{t,1}\overline{\Delta}p_{t,2}\rangle$ value.

In order to visualize the full correlation structure for all charged pairs in the four-dimensional momentum subspace $(\eta_i, \eta_j, \phi_i, \phi_j)$ we construct the $\langle\overline{\Delta}p_{t,1}\overline{\Delta}p_{t,2}\rangle$ map as it can be seen in Fig.6.1.

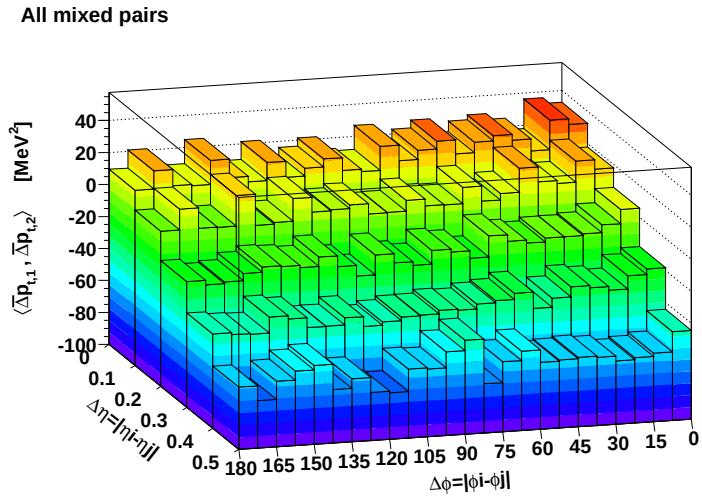


Figure 6.1: The $\langle\overline{\Delta}p_{t,1}\overline{\Delta}p_{t,2}\rangle$ map in $\Delta\eta$-$\Delta\phi$ space for all mixed pairs.

We observe a declination of the $\langle\overline{\Delta}p_{t,1}\overline{\Delta}p_{t,2}\rangle$ values with increasing $\Delta\eta$, leading to negative values (anticorrelation), showing a rather trivial effect of $p_T(\eta)$ dependence. As it can be seen in Fig.6.2, tracks with large separation in $\eta$ are anticorrelated in mean $p_T$.

Constructing the $\langle\overline{\Delta}p_{t,1}\overline{\Delta}p_{t,2}\rangle$ and the $\Sigma_{p_T}$ map for true pairs, as it is shown in Fig. 6.3, we also note the declination of the signal at finite $\Delta\eta$ which was reproduced with event mixing. The $\langle\overline{\Delta}p_{t,1}\overline{\Delta}p_{t,2}\rangle$ map was transformed to a $\Sigma_{p_T}$ map using the equations 3.14 and 3.19.

Thus, we should correct the maps taking into account the abovementioned $p_T(\eta)$ dependence by subtracting the map of the mixed pairs from that of true pairs. The results that will follow in the next sections present corrected $\langle\overline{\Delta}p_{t,1}\overline{\Delta}p_{t,2}\rangle$

and $\Sigma_{p_T}$ maps.

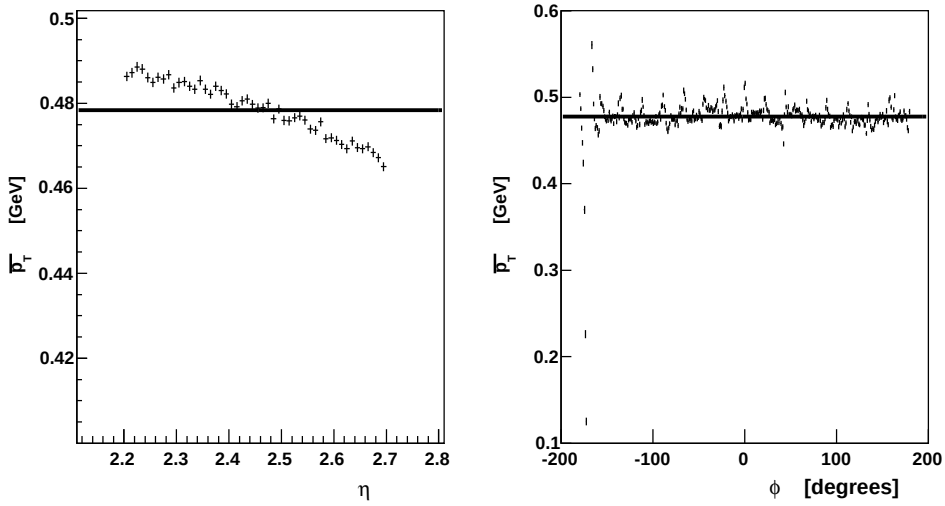


Figure 6.2: The dependence of the inclusive mean $p_T$ of positive particles, on $\eta$ and $\phi$ respectively.

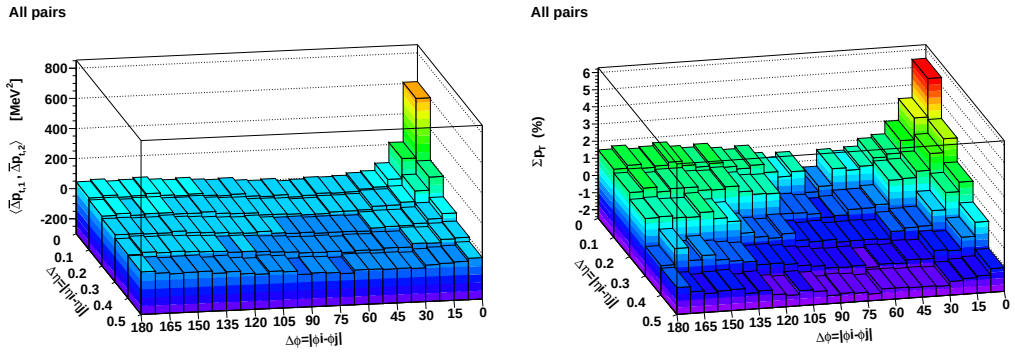


Figure 6.3: The $\langle \overline{\Delta}p_{t,1}\overline{\Delta}p_{t,2} \rangle$ (left panel) and the $\Sigma_{p_T}$ map (right panel) in $\Delta\eta$-$\Delta\phi$ space, for all true pairs uncorrected.

### Error estimates

For each bin, we calculate the average momentum correlator $\langle \overline{\Delta} p_{t,1} \overline{\Delta} p_{t,2} \rangle$ using the formula 3.14, because it provides a relatively easy way of estimating the statistical error compared to the transverse momentum covariance $\langle \langle \delta p_{t_i} \delta p_{t_j} \rangle_{i \neq j} \rangle$ which is a pair-measure (Eq. 3.15).

The statistical error on $\langle \overline{\Delta} p_{t,1} \overline{\Delta} p_{t,2} \rangle$ was estimated as follows. The value of $\langle \overline{\Delta} p_{t,1} \overline{\Delta} p_{t,2} \rangle$ was evaluated for each event of the whole sample of analyzed events and the dispersion ($D$) of the results was then calculated. The statistical error of $\langle \overline{\Delta} p_{t,1} \overline{\Delta} p_{t,2} \rangle$ was taken to be equal to $D/\sqrt{N_{events}}$.

In Fig. 6.4 we see the distributions of the $\langle \overline{\Delta} p_{t,1} \overline{\Delta} p_{t,2} \rangle$ taken from a sample of 3.5 million events and obtained using the mixed event analysis. We note that the obtained mean value is the one we use in the maps and the number of entries is the number of analyzed events.

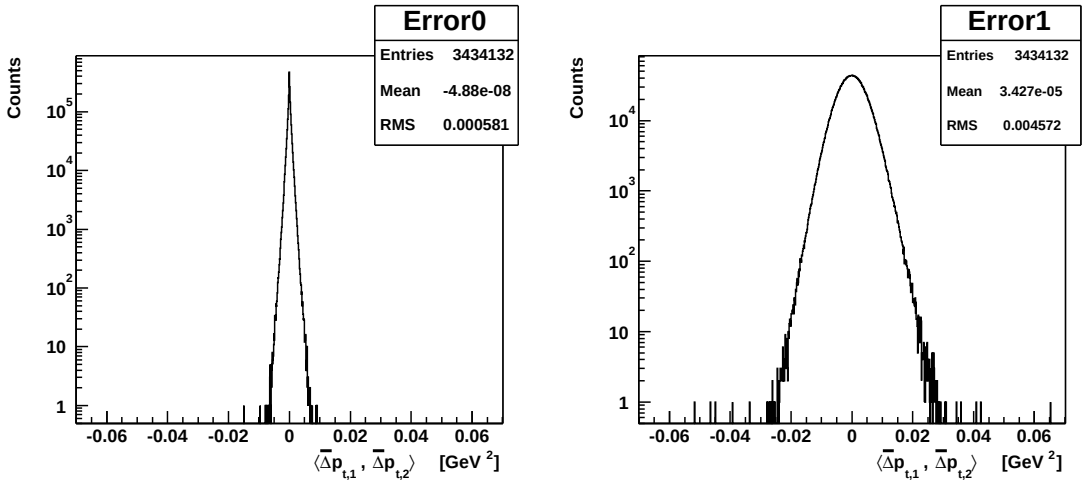


Figure 6.4: Distributions of the $\langle \overline{\Delta} p_{t,1} \overline{\Delta} p_{t,2} \rangle$ obtained using mixed events. The average value (left panel) and the correlator value at $0 < \Delta\eta < 0.1$ and $0 < \Delta\phi <$ 7.5 deg. (right panel) are given by the means of the distributions respectively.

Based on our results we find that the relation 3.16 holds extremely well.

**Two-track resolution**

Detector effects such as the finite two-track resolution influences the measured $\langle \overline{\Delta} p_{t,1} \overline{\Delta} p_{t,2} \rangle$ values. In order to estimate this contribution, an application of a cut in the opening angle distribution of true particle pairs detected in the TPC is needed. The exclusion of pairs with opening angle $\alpha \leq 10$ mrad affects only the magnitude of the signal placed at $0 \leq \Delta\phi \leq 7.5$ and $0 \leq \Delta\eta \leq 0.1$. The value of the correlator in this region drops from 608 MeV$^2$ (Fig. 6.3) to 370 MeV$^2$, resulting to an average value of $19.03 \pm 0.7$ MeV$^2$. The results that will follow, are not corrected for two-track resolution and HBT/Coulomb correlations.

### 6.2.2 Same event analysis

The $\langle \overline{\Delta} p_{t,1} \overline{\Delta} p_{t,2} \rangle$ map in $\Delta\eta$-$\Delta\phi$ space for all pairs is shown in Fig.6.5.

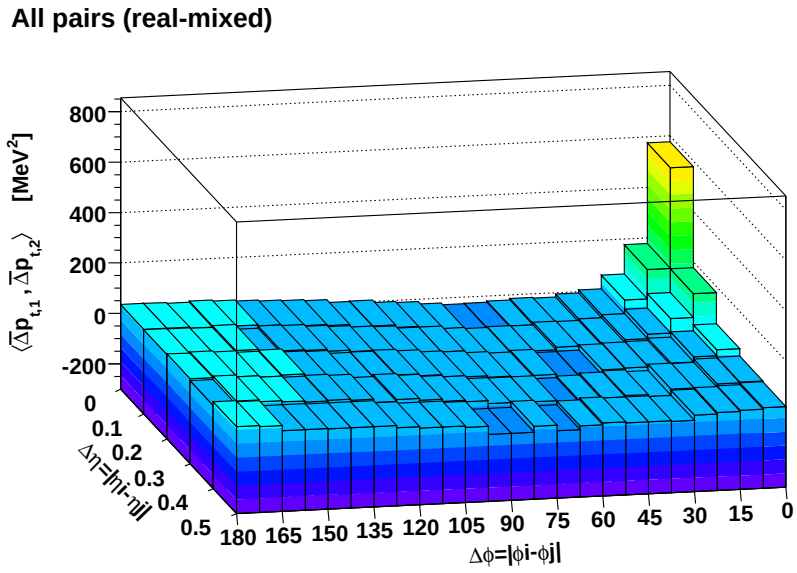


Figure 6.5: The $\langle \overline{\Delta} p_{t,1} \overline{\Delta} p_{t,2} \rangle$ map in $\Delta\eta$-$\Delta\phi$ space for all true-mixed pairs.

The same $\langle \overline{\Delta} p_{t,1} \overline{\Delta} p_{t,2} \rangle$ map can be plotted in a different way as the $\Delta\phi$ dependence of the $\langle \overline{\Delta} p_{t,1} \overline{\Delta} p_{t,2} \rangle$ in 5 slices of $\Delta\eta$, as can be seen in Fig.6.6. The line is a constant fit which provides the average value of the $\langle \overline{\Delta} p_{t,1} \overline{\Delta} p_{t,2} \rangle$ in the total momentum subspace $(\eta, \phi)$. The average value is consistent with the $\langle \overline{\Delta} p_{t,1} \overline{\Delta} p_{t,2} \rangle$ in

the total subspace as well as with the $\sigma^2_{p_T,dyn}$, as it can be calculated according to the Eq.3.11 (presented in section 6.1). Statistical errors for the $\langle \overline{\Delta} p_{t,1} \overline{\Delta} p_{t,2} \rangle$ map are uniform on $\Delta\phi$ (periodic variable) but as $\Delta\eta$ increases from 0.1 to 0.5 (finite $\eta$ acceptance), they get values from 3.5 to 11.5 MeV$^2$. The error of the corrected $\langle \overline{\Delta} p_{t,1} \overline{\Delta} p_{t,2} \rangle$ for each bin was calculated by adding in squares the statistical error of the real and the statistical error of the mixed value.

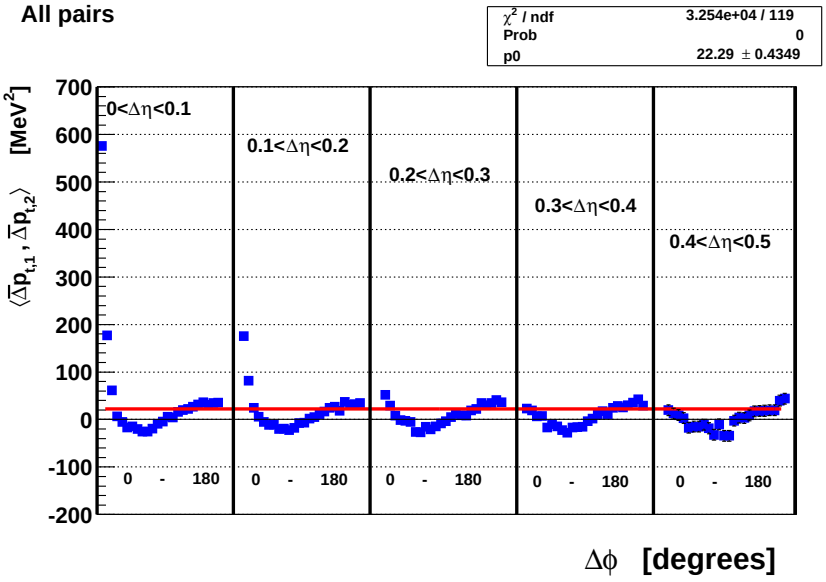


Figure 6.6: The $\Delta\phi$ dependence of the $\langle \overline{\Delta} p_{t,1} \overline{\Delta} p_{t,2} \rangle$ in 5 slices of $\Delta\eta$, for all pairs. The line is a constant fit.

The number of pairs depends strongly on the $\Delta\eta$ while is uniform on $\Delta\phi$, as it can be seen in Fig. 6.7. We note that in the bin of the map at $0 < \Delta\eta < 0.1$ and $0 < \Delta\phi < 7.5$ deg., there are more pairs than in the other bins at the same $\eta$ range, indicating a correlation.

The $\langle \overline{\Delta} p_{t,1} \overline{\Delta} p_{t,2} \rangle$ map contains two features: a rather narrow **near-side** component ($\Delta\phi \leq 30$ and $\Delta\eta \leq 0.3$) and a broad **away-side** component ($135 \leq \Delta\phi \leq 180$ and $\Delta\eta \leq 0.4$). The near-side peak is probably dominated by HBT (quantum) and Coulomb correlations. Bose and Fermi statistics, final state interactions and experimental effects such as the finite two-track resolution are the origin of short-range (anti-) correlations (SRC). SRC correlations show up

at small momentum differences $q$ and contribute significantly in the part of the map where $\Delta\phi \leq 45$ (this has been confirmed by applying a cut at pairs with $q_{inv} < 70$ MeV/c, where the four-momentum difference $q_{inv} \equiv \sqrt{\mathbf{q}^2 - {q_0}^2}$, is the momentum difference in the pair rest frame, $\mathbf{q}$ and $q_0$, are the differences in three-momentum and energy of a particle pair assuming the pion mass for each particle).

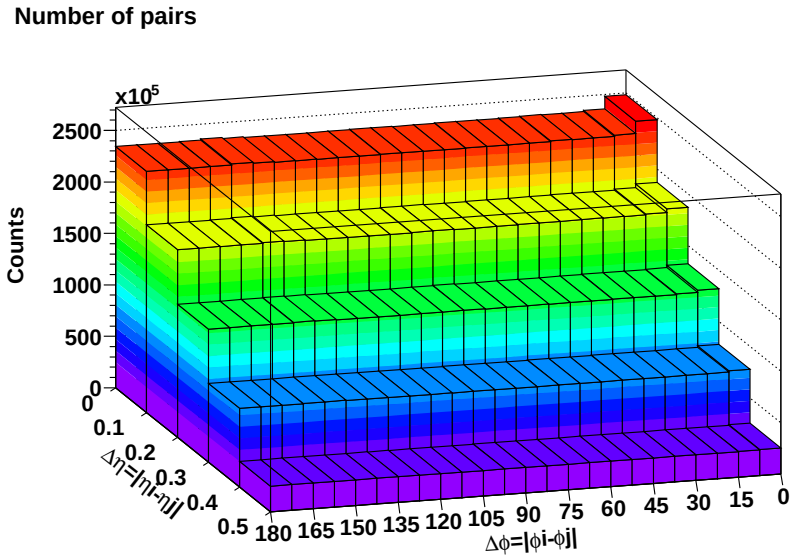


Figure 6.7: The number of pairs in $\Delta\eta$-$\Delta\phi$ space.

Long-range correlations (LRC) occur as a consequence of energy and momentum conservation and they are not localized at the origin. In the observed away-side peak, contribution by mini-jets and elliptic flow [70] is expected.

Fig.6.8 shows how the normalized fluctuation $\Sigma_{p_T}$ looks like in $\Delta\eta$-$\Delta\phi$ space for all pairs. Thus, the observed fluctuations at SPS which are about 1 % on average, have also a rich structure in momentum subspace, providing a signal that varies from -1 to 5.5 %. The landscape is dominated by a near-side peak symmetric about $\Delta\eta = \Delta\phi = 0$ and a broad $\Delta\eta$ independent away-side ridge.

Since particles from jet fragmentation cluster together in phase space, the two-particle correlation is expected to be enhanced. In particular, two-particle correlation at large $p_T$ in the azimuthal angle difference $\Delta\phi$ should be strongly peaked

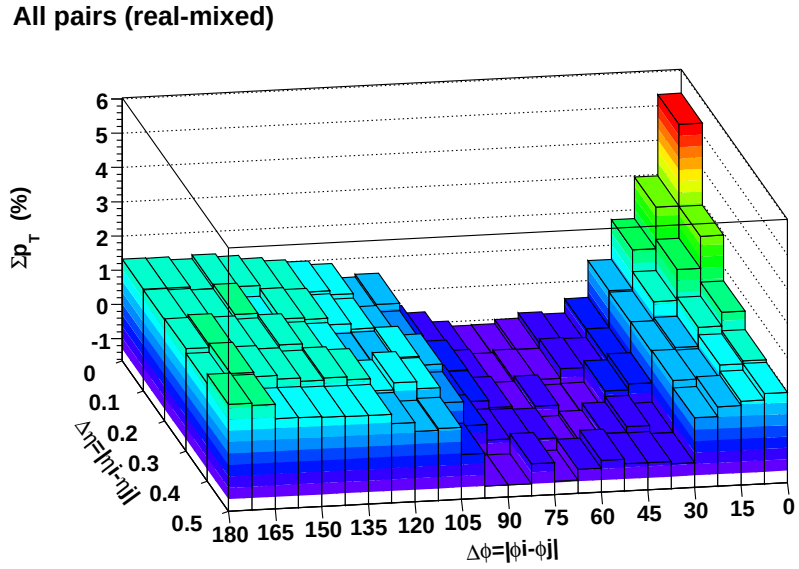


Figure 6.8: The $\Sigma_{p_T}$ map in $\Delta\eta$-$\Delta\phi$ space for all pairs.

at both forward ('near-side') $\Delta\phi = 0$, and backward ('back-to-back') $\Delta\phi = \pi$ directions. That mini-jet component should be invariant on $\Delta\eta$ (characteristic of back-to-back jet fragments).

### $\langle\overline{\Delta}p_{t,1}\overline{\Delta}p_{t,2}\rangle$ maps for different charge combinations.

The inclusive results of mean $p_T$ fluctuations for different charge combinations were presented in Table 6.1 (section 6.1).

In order to visualize the full correlation structure for like-sign and unlike-sign pairs in the four-dimensional momentum subspace $(\eta_i, \eta_j, \phi_i, \phi_j)$, we construct the $\langle\overline{\Delta}p_{t,1}\overline{\Delta}p_{t,2}\rangle$ map as it can be seen in Fig. 6.9. For the calculation of $\langle\overline{\Delta}p_{t,1}\overline{\Delta}p_{t,2}\rangle$ we used the Eq.3.17 and 3.18

The fact that the maps of positively and negatively charged particles look similar in strenght and shape at small $\Delta\phi$ and $\Delta\eta$, can be related to their common origin (HBT/Coulomb correlations). On the contrary, unlike-sign pairs have a peak at that region which is weaker and narrower, where we can expect contribution from Coulomb, resonances and $e^+e^-$ decays (conversion electron pairs).

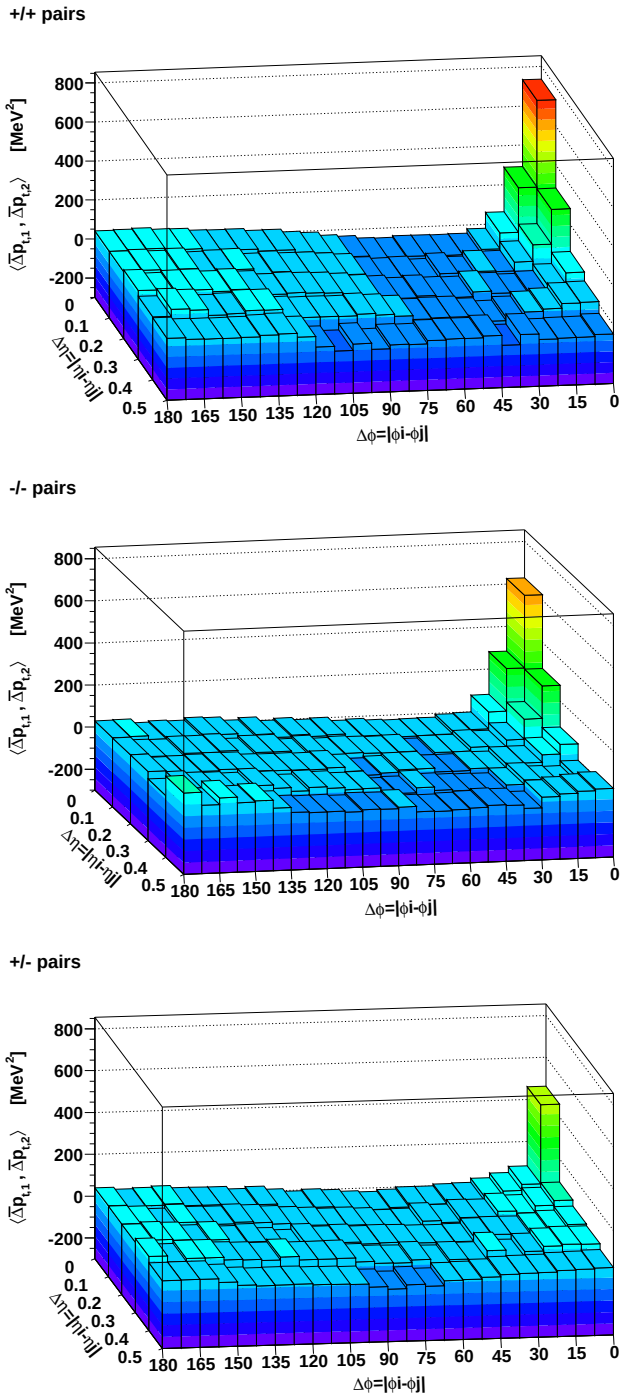


Figure 6.9: The $\langle \overline{\Delta} p_{t,1} \overline{\Delta} p_{t,2} \rangle$ map in $\Delta\eta$-$\Delta\phi$ space for positive, negative and unlike-sign pairs respectively.

### 6.2.3 Centrality dependence

Fig.6.10 (left panel) presents our measurement of $\langle\overline{\Delta}p_{t,1}\overline{\Delta}p_{t,2}\rangle$ in 158 A·GeV/c Pb-Au collisions as function of the mean number of participating nucleons $\langle N_{part}\rangle$. One observes that the correlator $\langle\overline{\Delta}p_{t,1}\overline{\Delta}p_{t,2}\rangle$ is finite and positive at this energy and that it exhibits a qualitative inverse proportionality to $\langle N_{part}\rangle$. This qualitative dependence is known to arise from the progressive dilution of the correlation with increased number of particle sources.

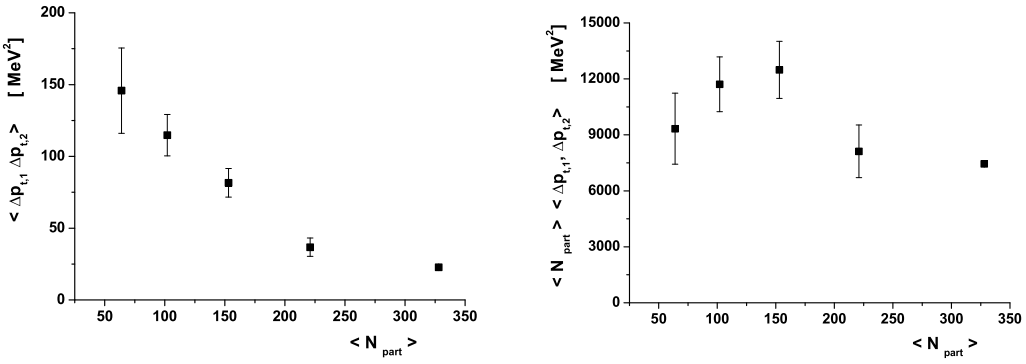


Figure 6.10: Measured correlator $\langle\overline{\Delta}p_{t,1}\overline{\Delta}p_{t,2}\rangle$ versus centrality and $\langle\overline{\Delta}p_{t,1}\overline{\Delta}p_{t,2}\rangle$ scaled by number of participating nucleons.

We next study the monotonic decrease of the correlator $\langle\overline{\Delta}p_{t,1}\overline{\Delta}p_{t,2}\rangle$ with increasing number of participating nucleons. As it was discussed in section 4.3, considering that if Pb-Au collisions consisted of a superposition of independent *nucleon-nucleon* interactions, with no rescattering of secondaries, the correlator measured at a given centrality in *A-A* should be proportional to the correlator measured in *p-p* and inversely proportional to the number of *nucleon-nucleon* interactions at the given centrality. In such collision scenario, the produced particle multiplicity should be stricly proportional to the number of interactions.

Thus, we scale the measured correlator $\langle\overline{\Delta}p_{t,1}\overline{\Delta}p_{t,2}\rangle$ by $\langle N_{part}\rangle$ to remove the $1/N$ correlation dilution, implying the assumption that the number of produced particles is roughly proportional to $\langle N_{part}\rangle$. Fig.6.10 (right panel) presents the scaled correlation $\langle N_{part}\rangle\langle\overline{\Delta}p_{t,1}\overline{\Delta}p_{t,2}\rangle$ as a function of participating nucleons. As a first observation, we note that, at variance with expectations based on an indepen-

dent *nucleon-nucleon* collision scenario, the scaled correlator $\langle N_{part}\rangle\langle\overline{\Delta}p_{t,1}\overline{\Delta}p_{t,2}\rangle$ varies strongly with collision centrality. Therefore, violation of the '$1/N$' scaling has been established and reveals a dramatic change that occurs in the collision dynamics of central Pb-Au collisions relative to peripheral Pb-Au and $p$-$p$ collisions. This observation is in qualitative aggreement with previous findings at RHIC using the same measure [67].

A summary of mean $p_T$ fluctuations for all pairs at $0.1 < p_T < 1.5$ GeV/c, $2.2 < \eta < 2.7$ and full $\phi$ acceptance at 158 A·GeV/c for five centrality classes is presented in Table 6.2.

The $\langle\overline{\Delta}p_{t,1}\overline{\Delta}p_{t,2}\rangle$ maps in $\Delta\eta$-$\Delta\phi$ space for these centrality classes are shown in Fig.6.11. We note that the peak structure is enhanced with centrality but the poor statistics of the data that come from the minimum bias run lead to a large fluctuation of the signal. Therefore, we examine the $\Delta\phi$ dependence of the correlator $\langle\overline{\Delta}p_{t,1}\overline{\Delta}p_{t,2}\rangle$ at $\Delta\phi = 30$ degrees and $0 < \Delta\eta < 0.5$, for true and mixed pairs respectively, as it can be seen in Fig.6.12. At $0 < \Delta\phi < 30$ and $120 < \Delta\phi < 180$, we observe a positive increase of the measured correlator with centrality (using mixed pairs there is a consistency to zero).

The centrality dependence of the measured correlator $\langle\overline{\Delta}p_{t,1}\overline{\Delta}p_{t,2}\rangle$, scaled by number of participating nucleons, for several regions of $\Delta\phi$ is shown in Fig.6.13. Since the overall fluctuations seem to be dominated by the short range and the away-side two-particle correlations, we can analyse separately these two components and observe their non-monotonic centrality dependence (two upper sets of points in Fig. 6.13).

The region of $30^o < \Delta\phi < 60^o$ is free of the influence of the two mentioned components and elliptic flow does not matter. The $p_T$ fluctuations in this region turn out to be close to zero and independent on centrality within the error bars. We also note an anticorrelation for all centrality classes in the region of $60^o < \Delta\phi < 90^o$.

It has been shown that $\langle\overline{\Delta}p_{t,1}\overline{\Delta}p_{t,2}\rangle$ is a nonmonotonic function of centrality. Such a behavior strongly resembles the dependence of the magnitude of collective flow $-directed(v_1)$ and $elliptic(v_2)-$ on $\langle N_{part}\rangle$. Thus, there is a natural suggestion that the $p_T$ fluctuations measured by $\langle\overline{\Delta}p_{t,1}\overline{\Delta}p_{t,2}\rangle$ may be caused by the collective flow. This suggestion is checked in the next subsection 6.2.4.

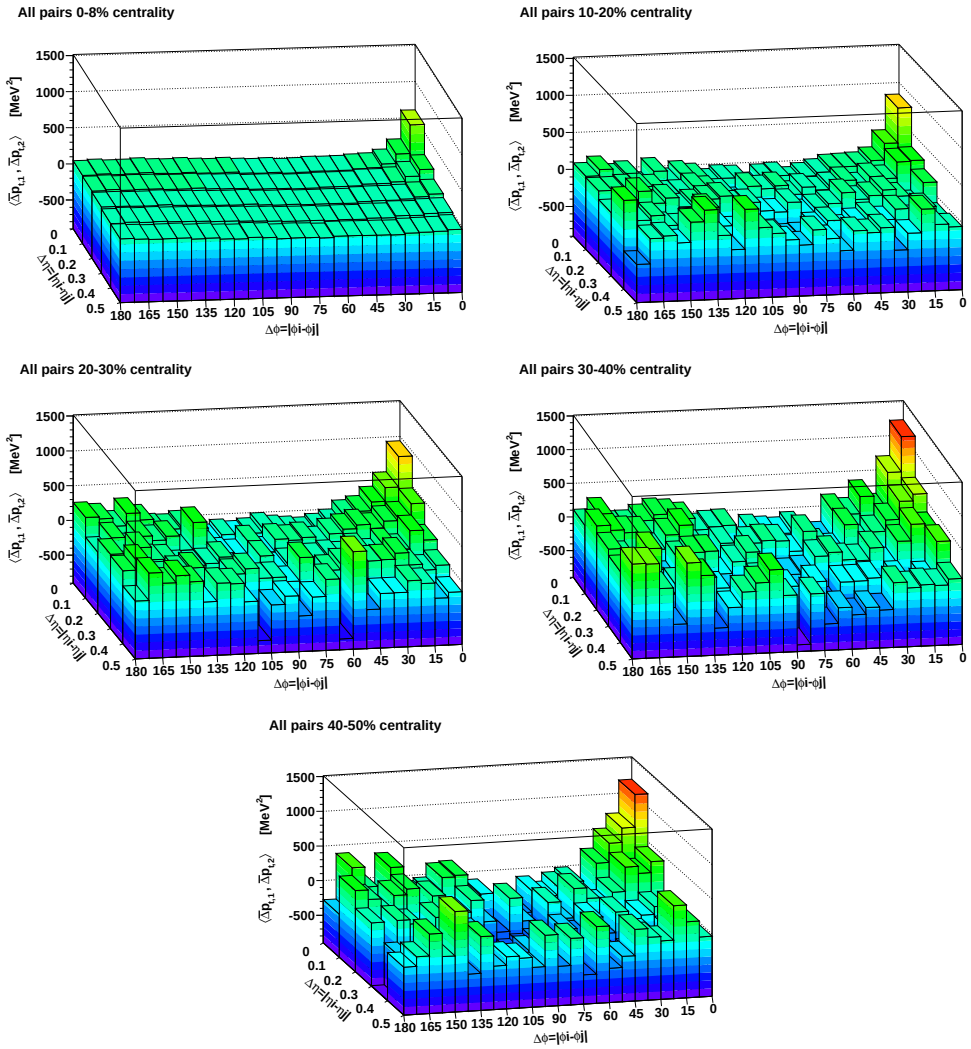


Figure 6.11: $\langle \overline{\Delta} p_{t,1} \overline{\Delta} p_{t,2} \rangle$ maps in $\Delta\eta$-$\Delta\phi$ space for five centrality classes.

| Centrality[%] | $0-8$ |
|---|---|
| $\langle\overline{\Delta}p_{t,1}\overline{\Delta}p_{t,2}\rangle[MeV^2]$ | $22.71 \pm 0.32$ |
| $\sigma^2_{p_T,dyn}[MeV^2]$ | $21.98 \pm 0.44$ |
| $n$ | 10003672 |
| $\langle N\rangle$ | $154.83 \pm 0.01$ |
| $\overline{p_T}$ [MeV/c] | $449.82 \pm 0.01$ |
| Centrality[%] | $10-20$ |
| $\langle\overline{\Delta}p_{t,1}\overline{\Delta}p_{t,2}\rangle[MeV^2]$ | $36.74 \pm 6.39$ |
| $\sigma^2_{p_T,dyn}[MeV^2]$ | $35.52 \pm 8.61$ |
| $n$ | 40146 |
| $\langle N\rangle$ | $104.81 \pm 0.1$ |
| $\overline{p_T}$ [MeV/c] | $448.52 \pm 0.14$ |
| Centrality[%] | $20-30$ |
| $\langle\overline{\Delta}p_{t,1}\overline{\Delta}p_{t,2}\rangle[MeV^2]$ | $81.61 \pm 9.99$ |
| $\sigma^2_{p_T,dyn}[MeV^2]$ | $68.62 \pm 12.7$ |
| $n$ | 39496 |
| $\langle N\rangle$ | $73.37 \pm 0.08$ |
| $\overline{p_T}$ [MeV/c] | $445.31 \pm 0.17$ |
| Centrality[%] | $30-40$ |
| $\langle\overline{\Delta}p_{t,1}\overline{\Delta}p_{t,2}\rangle[MeV^2]$ | $114.81 \pm 14.41$ |
| $\sigma^2_{p_T,dyn}[MeV^2]$ | $95.81 \pm 18.81$ |
| $n$ | 39763 |
| $\langle N\rangle$ | $50.07 \pm 0.07$ |
| $\overline{p_T}$ [MeV/c] | $441.57 \pm 0.2$ |
| Centrality[%] | $40-50$ |
| $\langle\overline{\Delta}p_{t,1}\overline{\Delta}p_{t,2}\rangle[MeV^2]$ | $145.79 \pm 29.73$ |
| $\sigma^2_{p_T,dyn}[MeV^2]$ | $129.62 \pm 35.69$ |
| $n$ | 38197 |
| $\langle N\rangle$ | $32.72 \pm 0.06$ |
| $\overline{p_T}$ [MeV/c] | $436.17 \pm 0.25$ |

Table 6.2: Summary of mean $p_T$ fluctuations for all pairs at $0.1 < p_T < 1.5$ GeV/c, $2.2 < \eta < 2.7$ and full $\phi$ acceptance at 158 A·GeV/c for five centrality classes. Errors are statistical only. The fluctuations are not corrected for two-track resolution and HBT/Coulomb correlations.

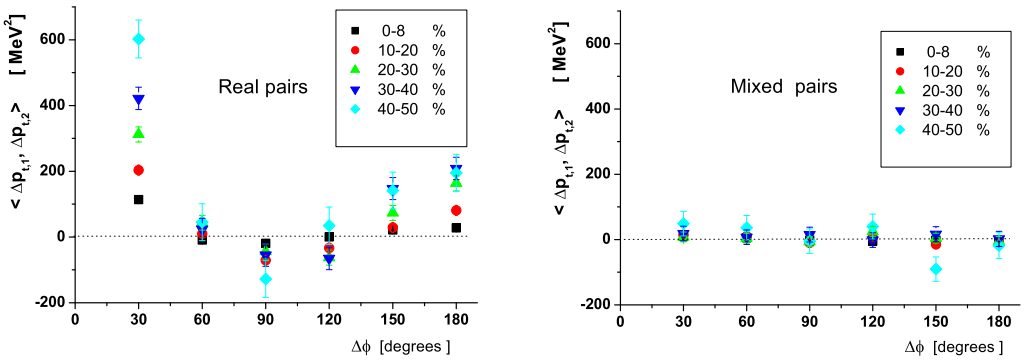


Figure 6.12: The $\Delta\phi$ dependence of the correlator $\langle \overline{\Delta} p_{t,1} \overline{\Delta} p_{t,2} \rangle$ for five centrality classes, for real and mixed pairs respectively.

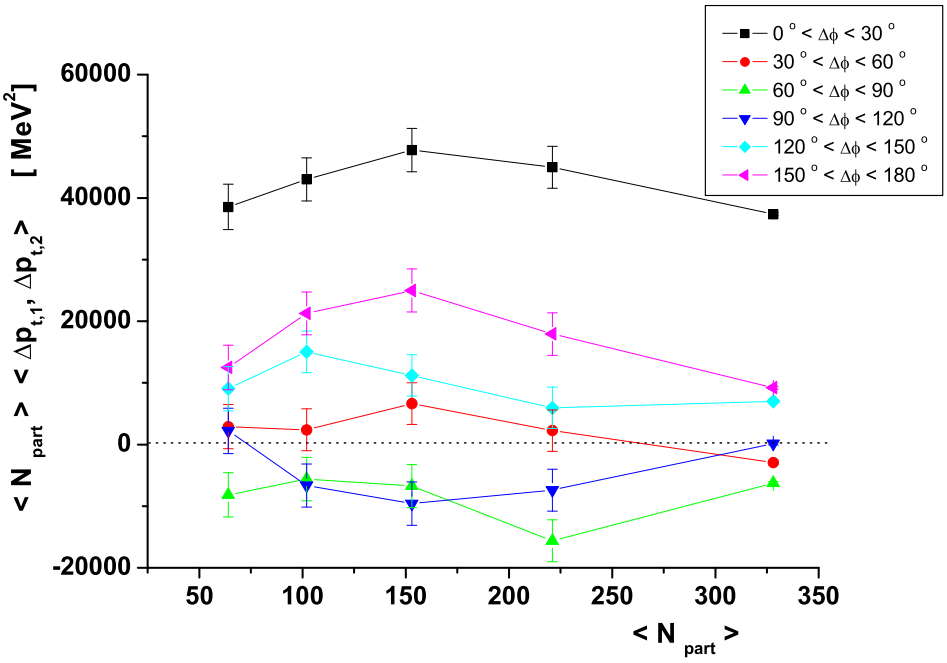


Figure 6.13: Centrality dependence of the measured correlator $\langle \overline{\Delta} p_{t,1} \overline{\Delta} p_{t,2} \rangle$, scaled by number of participating nucleons, for several regions of $\Delta\phi$.

### 6.2.4 Elliptic flow contribution

In addition to correlations due to SRC and jets, the two-particle azimuthal distributions expressed via the momentum correlator in $MeV^2$, exhibit a structure attributable to an elliptic flow anisotropy of single particle production relative to the reaction plane [68, 69]. This leads to a two-particle azimuthal distribution of the form of the Eq. 6.3

$$\frac{dN}{d\Delta\phi} \equiv B[1 + 2v_2^2 cos(2\Delta\phi)] \tag{6.3}$$

where $v_2$ is the elliptic flow parameter and $B$ a normalization constant [70]. Previous measurements [69] using several methods have shown that sizable $v_2$ values persist to high $p_T$.

The value of $v_2$ as a function of centrality and $p_T$ has been measured by the CERES experiment [71].

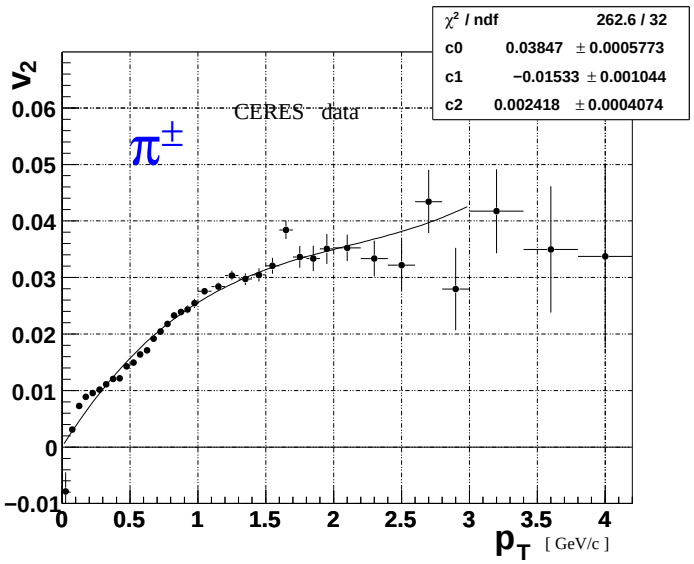


Figure 6.14: $\pi$ elliptic flow measured by CERES at $\langle\sigma/\sigma_{geo}\rangle = 8.9$ % [72].

The elliptic flow of pions measured by CERES at $\langle\sigma/\sigma_{geo}\rangle = 8.9$ % [72] is shown in Fig. 6.14. Since $v_2$ can be expressed as a function of $p_T$ , we introduce the measure $f_{i,j}$ as:

$$f_{i,j} \equiv 1 + 2v_2(p_{Ti})v_2(p_{Tj})cos(2|\phi(i) - \phi(j)|) \tag{6.4}$$

Then, we calculate the average momentum correlator $\langle \overline{\Delta} p_{t,1} \overline{\Delta} p_{t,2} \rangle$ for mixed events , multiplying the $p_T$ covariance with $f_{i,j}$ and weighting the numbers of pairs [73] as follows:

$$\langle \overline{\Delta} p_{t,1} \overline{\Delta} p_{t,2} \rangle_{mixed+flow} \equiv \frac{1}{n_{events}} \sum_{k=1}^{n_{events}} \left[ \frac{\sum_{i \neq j}^{N_k} (p_{Ti} - \overline{p_T})(p_{Tj} - \overline{p_T}) f_{i,j}}{\sum_{i \neq j}^{N_k} f_{i,j}} \right] \tag{6.5}$$

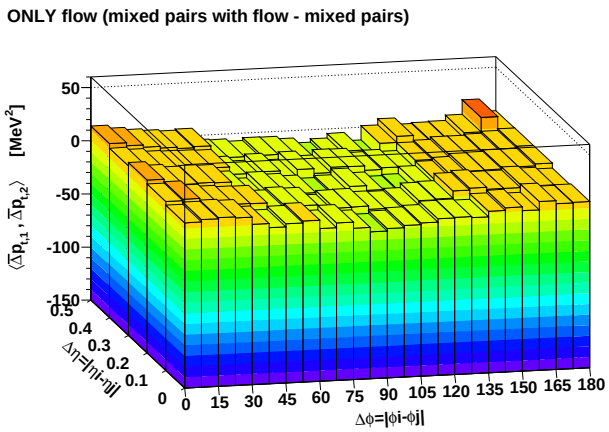


Figure 6.15: The $\langle \overline{\Delta} p_{t,1} \overline{\Delta} p_{t,2} \rangle$ map in $\Delta\eta$-$\Delta\phi$ space for all pairs assuming there is only flow, as can be obtained by subtracting the corresponding map of mixed pairs from the map of mixed pairs that have elliptic flow.

Subtracting the corresponding map of mixed pairs in the momentum subspace, from the map of mixed pairs that have elliptic flow calculated by Eq. 6.5, we can evaluate the elliptic flow expressed in units of $MeV^2$ as it can be seen in Fig. 6.15. The $\cos(2\Delta\phi)$ modulation introduced by the elliptic flow obtained at $0 < \Delta\eta < 0.1$ where the statistical error is smaller, is shown in the left panel of Fig. 6.16. In case the average value of $v_2$ ($\sim$ 1.5 % at this $p_T$ range and centrality) is used for the evaluation of $f_{i,j}$ and not the parametrized one, the $\langle \overline{\Delta} p_{t,1} \overline{\Delta} p_{t,2} \rangle$ does not change. The expected $\cos(2\Delta\phi)$ modulation comes through the $p_T$ dependence.

In order to confirm this effect, a Monte Carlo analysis was performed [74] , generating events with independent particles, following the measured inclusive $p_T$ distribution where the uniform azimuthal angle distribution of the events was modified by the elliptic flow expected by CERES according to the parametrization of $v_2(p_T)$ shown in Fig. 6.14 (right panel of Fig. 6.16). Both methods are in a good agreement but for our study we will use the value of the elliptic flow obtained by the calculation of $\langle \overline{\Delta} p_{t,1} \overline{\Delta} p_{t,2} \rangle_{mixed+flow}$.

Fig. 6.17 shows the $\Delta\phi$ dependence of the $\langle \overline{\Delta} p_{t,1} \overline{\Delta} p_{t,2} \rangle$ at $0 < \Delta\eta < 0.1$ with the expected elliptic flow superimposed, for all pairs. We can subtract the CERES flow from the $\langle \overline{\Delta} p_{t,1} \overline{\Delta} p_{t,2} \rangle$ map as it can be seen in Fig. 6.18 and correct as well as the normalized fluctuation $\Sigma_{p_T}$ (see Fig. 6.19).

Thus, one concludes that the effect of the azimuthal anisotropy caused by the elliptic flow is not responsible for the observed dynamical $p_T$ fluctuations. The question that remains is what is the origin of the observed broad away-side peak and whether is a low or a high $p_T$ effect.

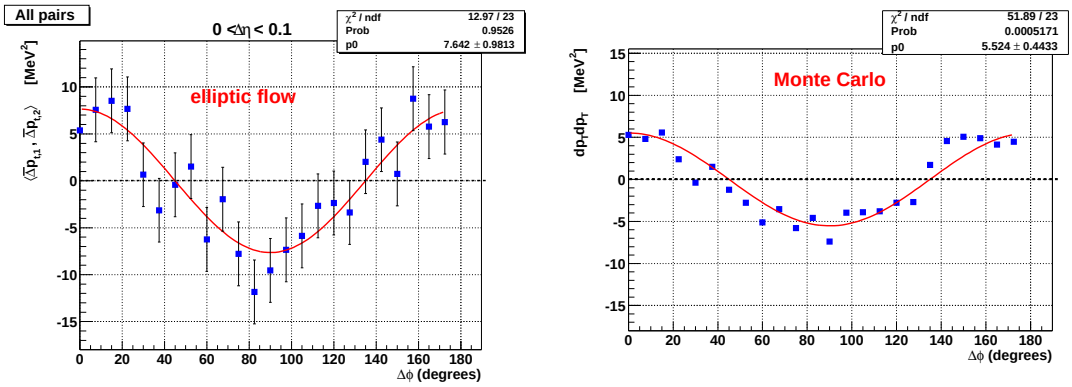


Figure 6.16: Estimation of the elliptic flow expected by CERES using mixed-event analysis (left panel) and Monte Carlo evaluation [74] (right panel).

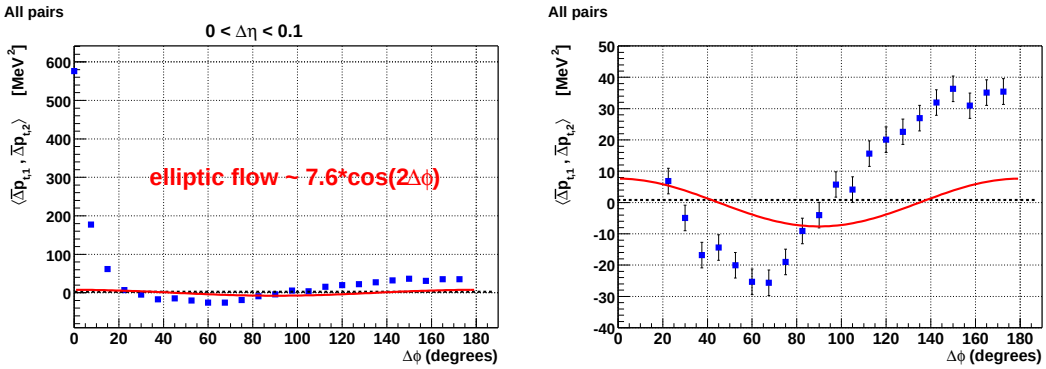


Figure 6.17: The $\Delta\phi$ dependence of the $\langle\overline{\Delta}p_{t,1}\overline{\Delta}p_{t,2}\rangle$ at $0 < \Delta\eta < 0.1$ with the expected elliptic flow superimposed, for all pairs.

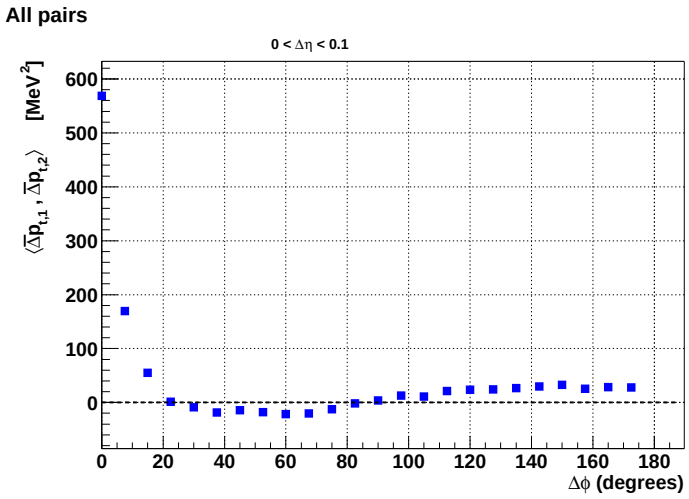


Figure 6.18: The $\Delta\phi$ dependence of the $\langle\overline{\Delta}p_{t,1}\overline{\Delta}p_{t,2}\rangle$ at $0 < \Delta\eta < 0.1$, for all pairs, after subtraction of the expected elliptic flow.

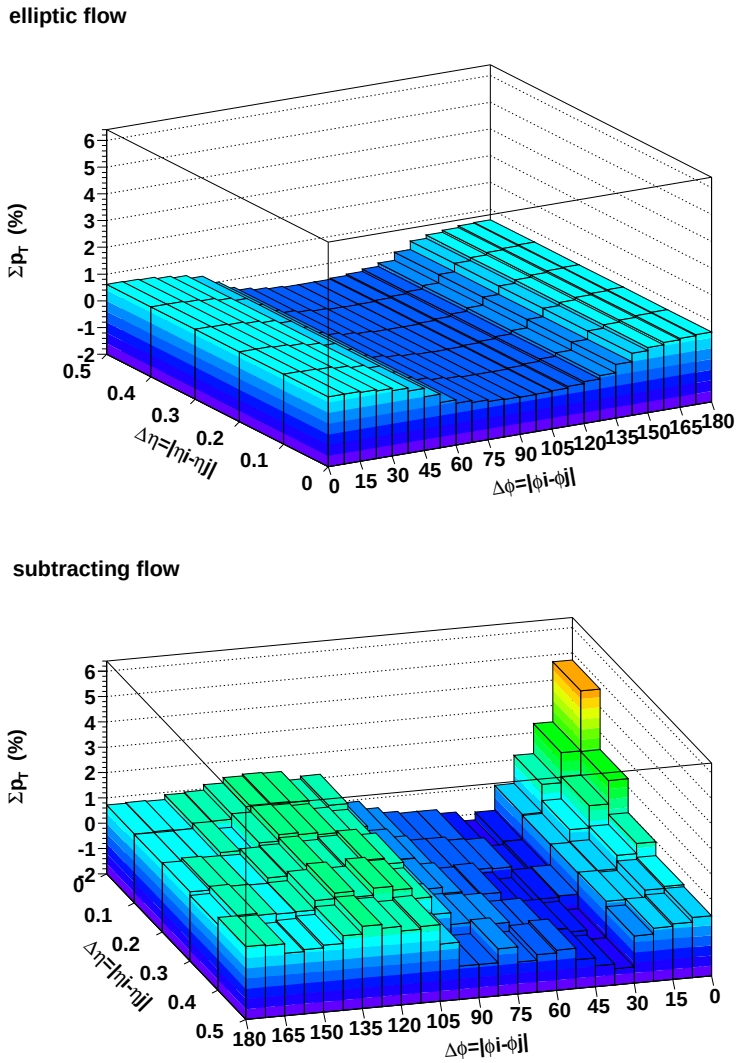


Figure 6.19: The $\Sigma_{p_T}$ map in $\Delta\eta$-$\Delta\phi$ space for all pairs, when only elliptic flow is present (top panel) and the total $\Sigma_{p_T}$, after subtraction of the expected elliptic flow (bottom panel).

## 6.3 Two-particle correlation analysis using the cumulant $p_T$ variable $x$

In order to achieve a better understanding of the fluctuation structure one needs to apply a more differential method. The correlations can be studied by plotting the cumulative $p_T$ variables of particle pairs. Namely, for a given particle, instead of its $p_T$ one introduces the variable $x$ defined as [42, 43, 44]:

$$x(p_T) = \int_0^{p_T} \rho(p_T^{'}) dp_T^{'} \tag{6.6}$$

where $\rho(p_T^{'})$ is the inclusive $p_T$ distribution, normalized to unity, which is obtained from all particles used in the analysis. By construction, the $x$ variable varies between 0 and 1 with a flat probability distribution. The Fig.6.20 shows the inclusive $p_T$ distribution and the corresponding $p_T$ variable $x$, for all pairs. Thus, a high $p_T$ value corresponds to a high $x$ (close to 1). We have also prepared the cumulant $p_T$ variable $x$ for different charge combinations.

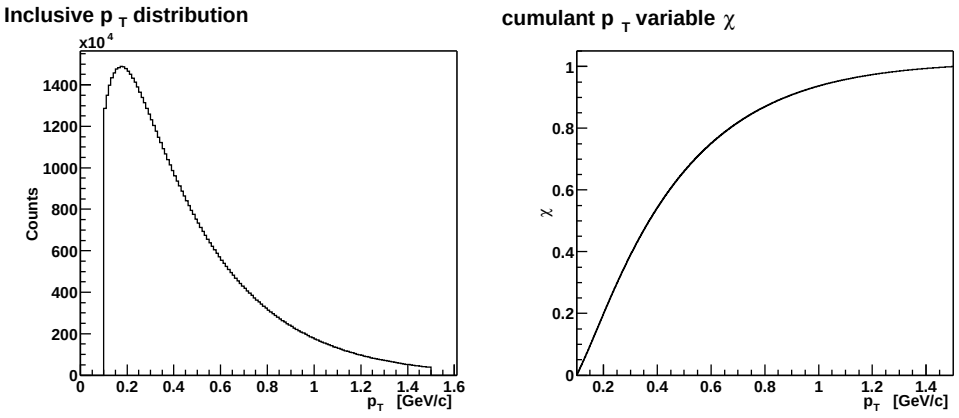


Figure 6.20: The inclusive $p_T$ distribution (left panel) and the corresponding $p_T$ variable $x$ (right panel), for all pairs.

The two-particle correlation plots, as presented in this work, are obtained by plotting $(x1, x2)$ points for all possible particle pairs within the same event. The number of pairs in each $(x1, x2)$ bin is divided by the mean number of pairs in a

bin (averaged over all $(x1, x2)$ bins). This two-dimensional plot is uniform when no inter-particle correlations are present in the system. Correlations due to the Bose statistics produce a ridge along the diagonal of the $(x1, x2)$ plot, which starts at (0, 0) and ends at (1, 1), whereas temperature fluctuations lead to a saddle shaped structure [39]. As will be seen in this section, the distribution of $x1$ or $x2$ obtained from the two-dimensional $(x1, x2)$ plots by projecting on the $x1$ or $x2$ axis is not flat. This is due to the method by which the plots are constructed. Namely, each pair of particles is represented by a point on the plot. Therefore, the events with higher multiplicities are represented by a larger number of pairs than those with smaller multiplicities. It should be stressed that in the absence of any correlations the $(x1, x2)$ plot is uniformly populated and the $x1$ and $x2$ projections are flat.

### 6.3.1 Two-particle correlation plots in several $\Delta\phi$ regions

A study of two-particle correlation plots from a sample of about seven millions events, having a centrality of the upper 8 % of the total geometric cross section, is performed in several $\Delta\phi$ regions.

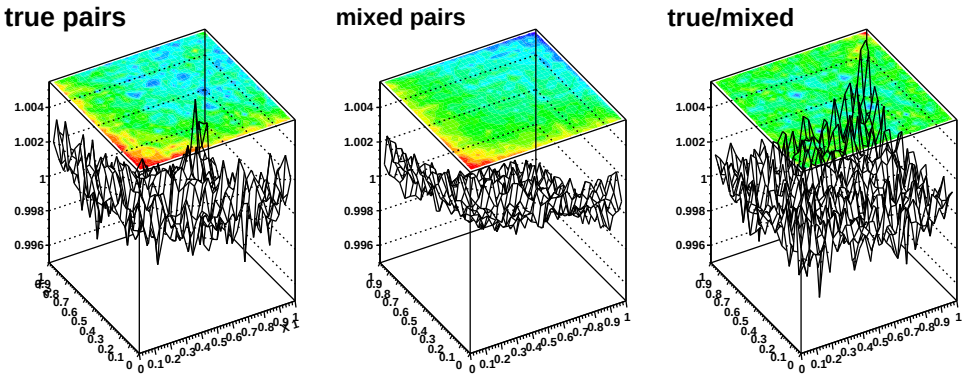


Figure 6.21: The two-particle correlation plots for all pairs, mixed pairs and true versus mixed, at $0 < \Delta\eta < 0.5$ and $142.5 < \Delta\phi < 150$ deg.).

The two-particle correlation plots for mixed pairs as it can be seen in Fig. 6.21 are not completely flat as it is expected by definition. Therefore, to mini-

mize instrumental effects and to reveal possibly the origin of the away-side peak that was observed using the $\langle\overline{\Delta}p_{t,1}\overline{\Delta}p_{t,2}\rangle$ measure, we construct the two-particle correlation plots for all pairs corrected, by dividing real versus mixed.

After each charged particle pair $(x1, x2)$ was entered into the plot, the bin contents were normalized by diving with the average number of entries per bin. The data in these figures, are plotted with same colour scales and are symmetric about the diagonal by construction. All the next plots are corrected after a division with the corresponding mixed ones.

Two-particle correlation plots using the cumulant $p_T$ variable $x$ for all pairs, in several $\Delta\phi$ regions, are given in Fig. 6.22. We note that the plots are not uniformly populated. Contributions to them include, but are not limited to, quantum statistics, Coulomb effects, resonances decays, instrumental effects and 'dynamical' fluctuations. At $0^o < \Delta\phi < 30^o$, one observes a prominent ridge along the main diagonal. At $30^o < \Delta\phi < 120^o$, the plots seem to be rather flat. At $120^o < \Delta\phi < 180^o$, we see a high-$p_T$ correlation given as a sharp narrow peak as an enhancement in the region close to $x1 = x2 = 1$. It was already presented before (see Fig. 6.12 for 0-8 % centrality) that the average momentum correlator $\langle\overline{\Delta}p_{t,1}\overline{\Delta}p_{t,2}\rangle$ in the same region ($120^o < \Delta\phi < 180^o$) is positive. This observation attributes the away-side peak of the $\langle\overline{\Delta}p_{t,1}\overline{\Delta}p_{t,2}\rangle$ in that $\Delta\phi$ region to high-$p_T$ correlations.

A separate treatment of positive, negative and unlike-signed pairs is generally necessary in order to extract complete information, since different physics may affect each combination. Two-particle correlation plots for all charged combinations are presented in Figs. 6.23, 6.24, 6.25. One oberves a ridge along the main diagonal for the like-signed pairs corresponding to quantum correlations and a peak in the unlike-signed pairs ($x1 = x2 = 0$) due to the Coulomb interaction.

In order to see how the elliptic flow influences the two-particle correlation plots, we use the same procedure described in 6.2.4. Thus, the flow is evaluated by giving a weight to mixed particle pairs equal to $f_{i,j}$ according to Eq. 6.4 and divide the resulting plots with the corresponding ones of mixed pairs. The results are presented in Fig. 6.26. The plots are flat indicating that the elliptic flow that is measured at CERES, is too weak to be visible. An abnormally large value of $3v_2$, where $v_2$ gets the measured by CERES parametrized value [72],

results to two-particle correlation plots with much bigger high-$p_T$ enhancement at $x1 = x2 = 1$, as can be seen in Fig. 6.27,

Two-particle correlation plots for all pairs in smaller $\Delta\phi$ bins, 24 in total, corresponding to an angle of 7.5 degrees (the bin index follows the increase of $\Delta\phi$, i.e., 1 bin corresponds to $0 < \Delta\phi < 7.5$, 2 bin corresponds to $7.5 < \Delta\phi < 15$, 24 bin corresponds to $172.5 < \Delta\phi < 180$, allowing a comparison with the measured $\langle \overline{\Delta} p_{t,1} \overline{\Delta} p_{t,2} \rangle$) can be found in appendix A.

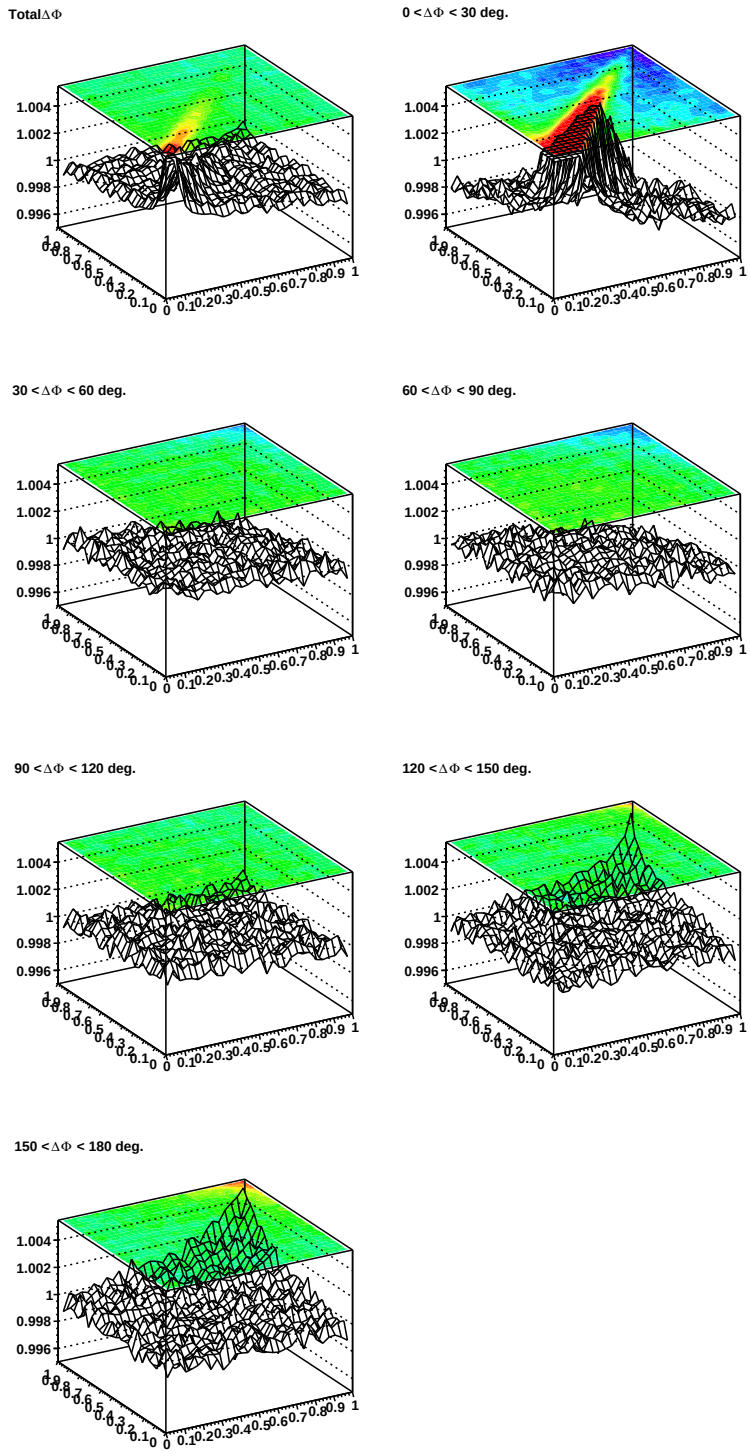


Figure 6.22: Two-particle correlation plots using the cumulant $p_T$ variable $x$ for all pairs, in several $\Delta\phi$ regions.

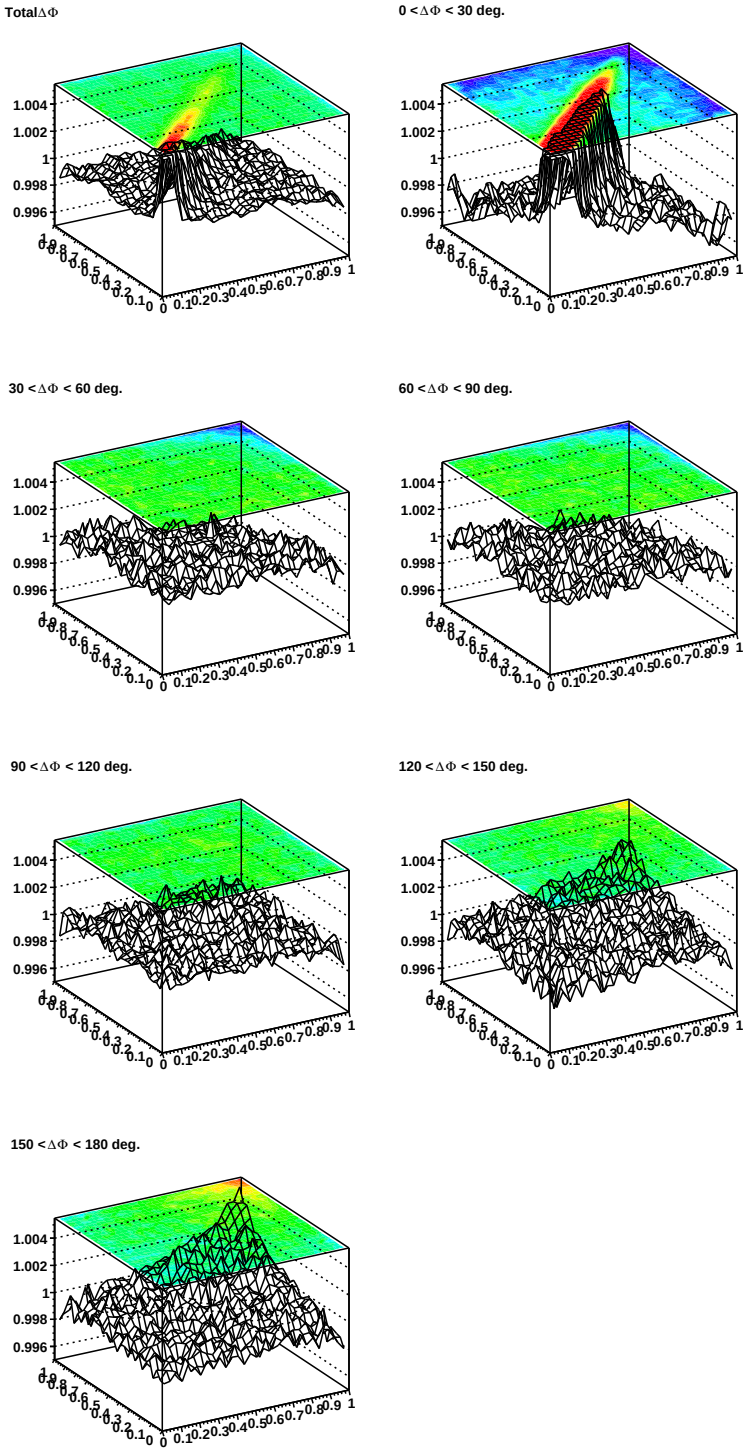


Figure 6.23: Two-particle correlation plots using the cumulant $p_T$ variable $x$ for positive pairs, in several $\Delta\phi$ regions.

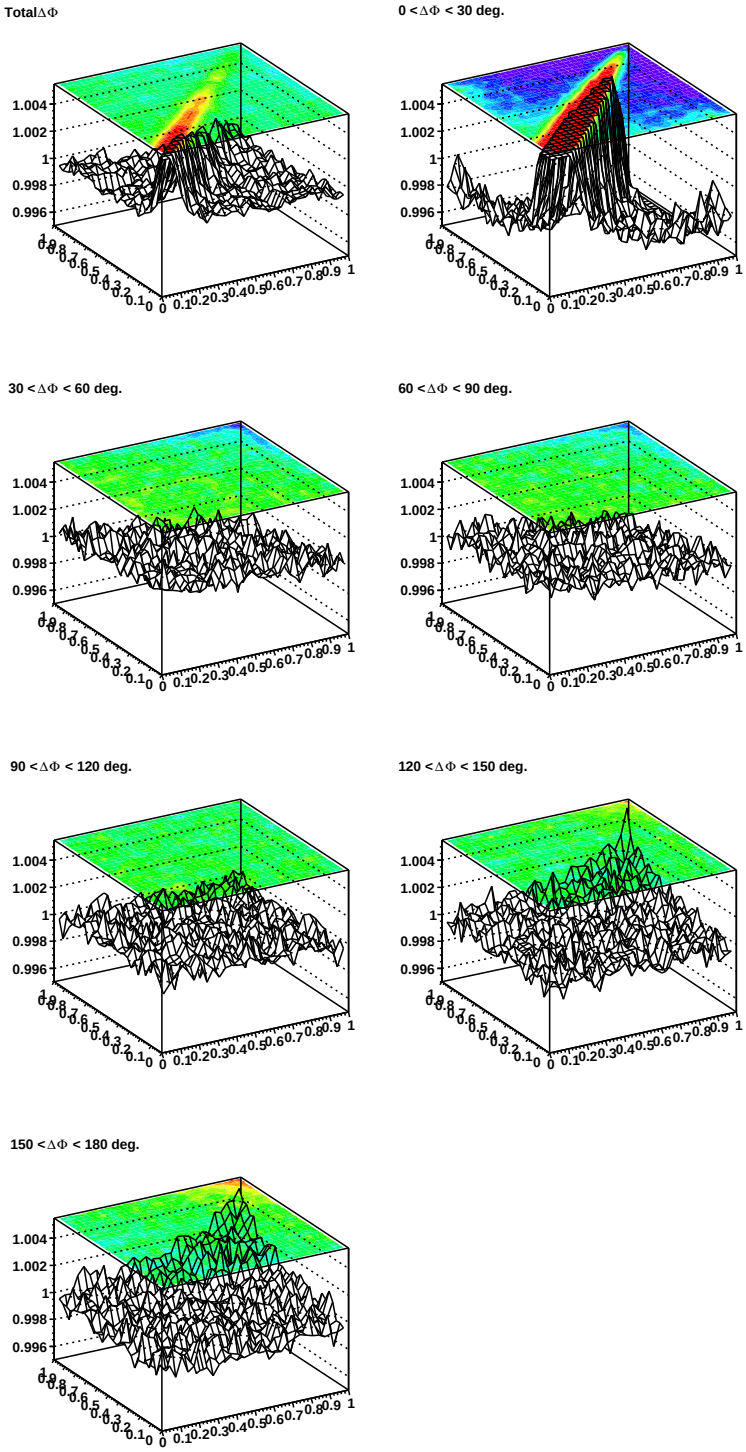


Figure 6.24: Two-particle correlation plots using the cumulant $p_T$ variable $x$ for negative pairs, in several $\Delta\phi$ regions.

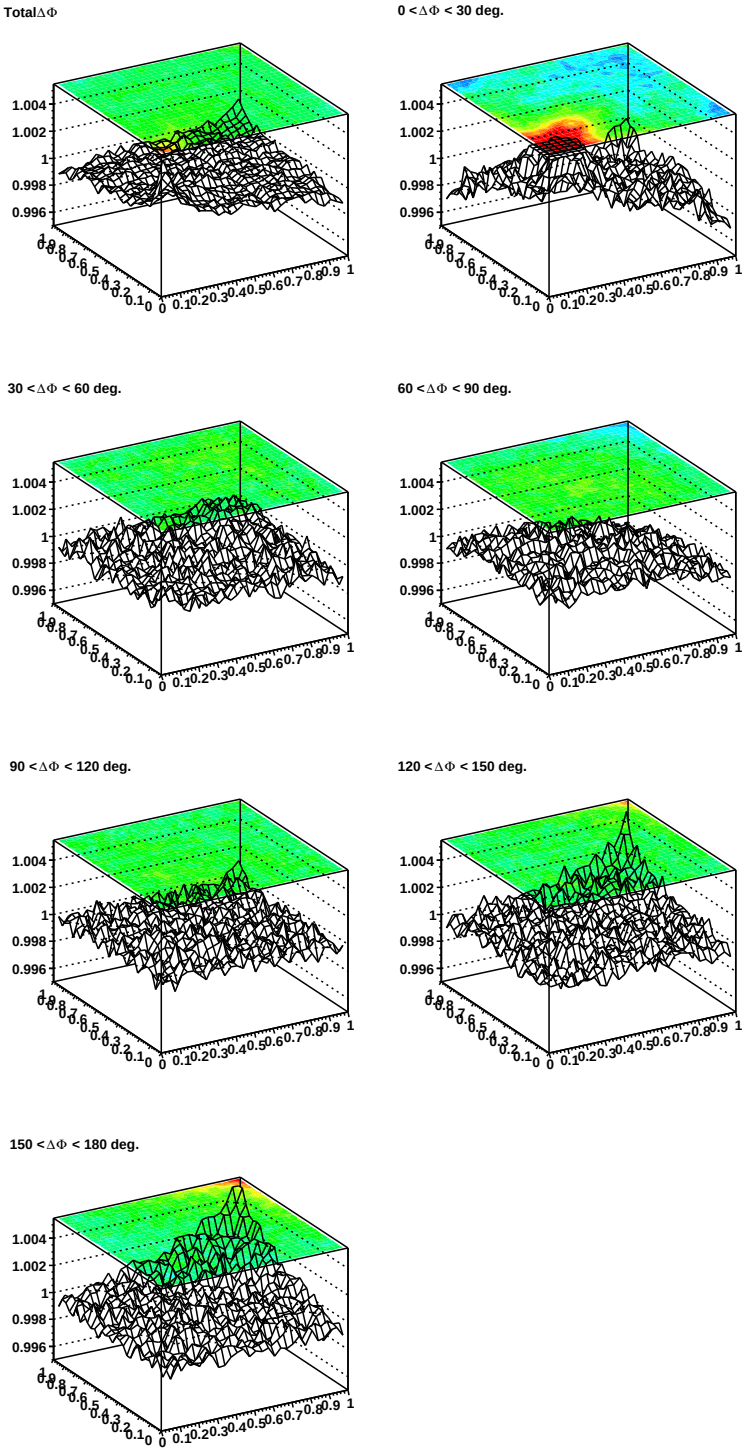


Figure 6.25: Two-particle correlation plots using the cumulant $p_T$ variable $x$ for unlike-sign pairs, in several $\Delta\phi$ regions.

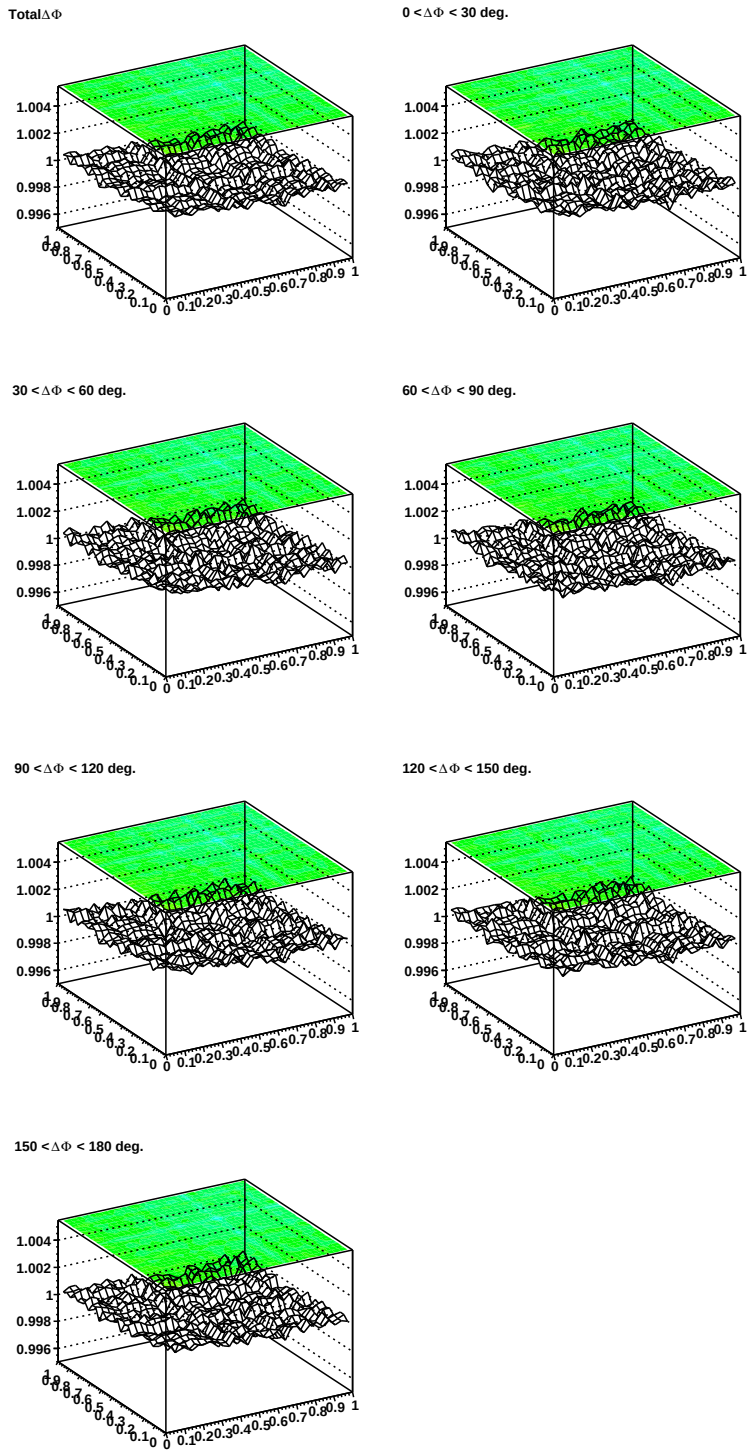


Figure 6.26: Two-particle correlation plots using the cumulant $p_T$ variable $x$ for all pairs that have only the elliptic flow expected by CERES (corrected by dividing mixed with flow versus mixed), in diferent $\Delta\phi$ regions.

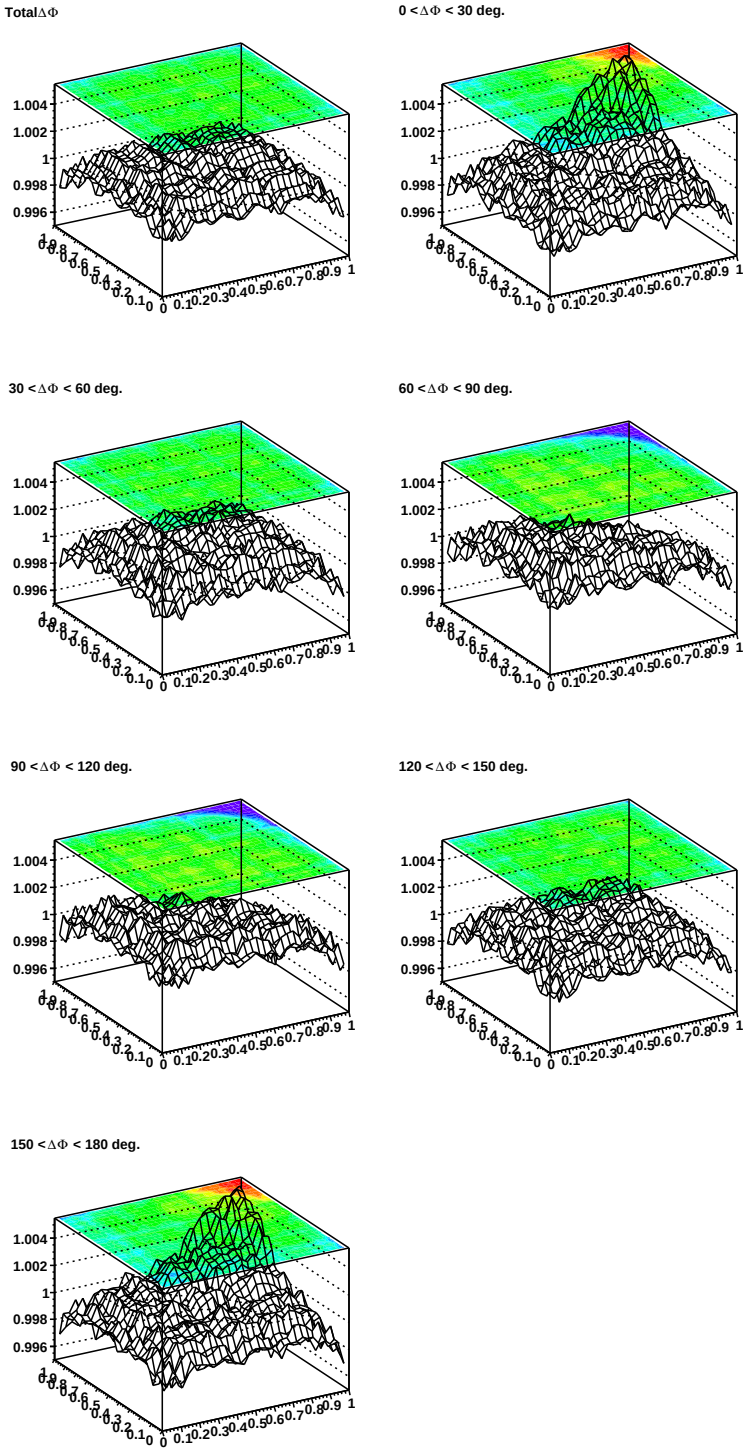


Figure 6.27: Two-particle correlation plots using the cumulant $p_T$ variable $x$ for all pairs that have only elliptic flow with $3v_2$, where $v_2$ gets the expected by CERES value (corrected by dividing mixed with flow versus mixed), in several $\Delta\phi$ regions.

## 6.4 Discussion

Enhanced event-by-event fluctuations of transverse momenta are considered to be one of the signatures of the vicinity to the critical point of the QCD phase transition. The fluctuations observed so far turned out to be rather independent of beam energy [45]. On the other hand, the fluctuations seem to be a non-monotonic function of centrality.

More insight into the origin of the observed fluctuations is gained by studying the average momentum correlator $\langle \overline{\Delta} p_{t,1} \overline{\Delta} p_{t,2} \rangle$ between pairs of tracks of a given opening angle. The covariance map (Fig. 6.5) reveals several structures and demonstrates that if the fluctuations were to be characterized by one single number the result would depend on the experiment's acceptance. The observed nonzero $p_T$ fluctuations indicate that particle $p_T$ is drawn event-wise from an effective parent distribution which deviates , as a function of $\Delta\phi, \Delta\eta$ and differently in each event, from the inclusive $p_T$ distribution.

The landscape is dominated by the short range correlation peak at small opening angles, most probably originating from Bose-Einstein and Coulomb effects between pairs of particles emitted with similar velocities, and the broad maximum at $\Delta\phi$=180° which contains back-to-back correlations like those observed at RHIC and the SPS [75]. The elliptic flow measured by CERES cannot explain the observed dynamical $p_T$ fluctuations. The non-monotonic centrality dependence of the overall fluctuations is indeed visible in the separate analysis of these two components. Since the critical point fluctuations should be present for all opening angles the best strategy seems to be to focus on the fluctuations in the region of $30° < \Delta\phi < 60°$, free of the influence of the two mentioned components, and where the elliptic flow cancels out.The $p_T$ fluctuations in this region turn out to be close to zero and independent on centrality.

Concerning the observed away-side peak, we demonstrated that it comes from high-$p_T$ correlations that cannot be attributed to the elliptic flow. The cumulative two-particle correlation study provides results that are consistent with those of the average momentum correlator $\langle \overline{\Delta} p_{t,1} \overline{\Delta} p_{t,2} \rangle$. Thus, we incline to consider the event-by-event fluctuations of mean transverse momentum mostly related to two-particle correlations.

The event and track selection criteria reduce the possible systematic bias of the measured $\langle \overline{\Delta} p_{t,1} \overline{\Delta} p_{t,2} \rangle$ values. Anyway, the remaining systematic uncertainty should be estimated varying the values of cut parameters within a reasonable range. It would also be interesting to analyze the beam energy dependence of this quantity, as well as following a similar procedure, like in case of elliptic flow, to remove Bose-Einstein and Coulomb effects and provide a 'clean' map from known correlations.